Article

Current Biology

RhoA Controls Axon Extension Independent of Specification in the Developing Brain

Graphical Abstract

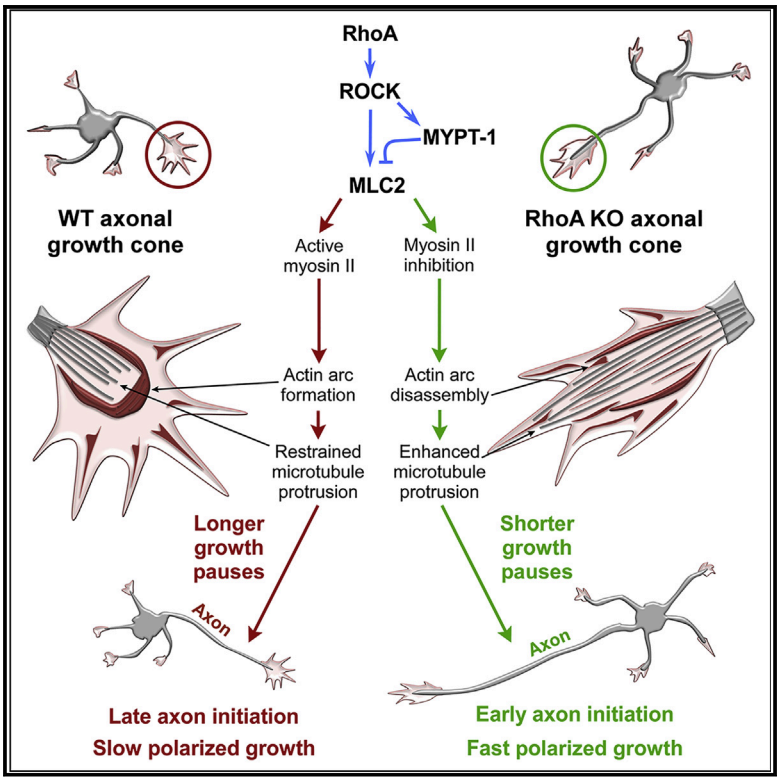

Highlights

- RhoA restrains axon initiation and growth independent of specification
- Myosin II is the physiological target of RhoA during axon growth
- RhoA/myosin-II-dependent actin arcs restrict microtubule advance in the growth cone
- RhoA instructs the duration of growth and pause phases in developing axons

Authors

Sebastian Dupraz, Brett J. Hilton, Andreas Husch, ..., Sina Stern, Cord Brakebusch, Frank Bradke

Correspondence

frank.bradke@dzne.de

In Brief

Combining genetic, molecular, pharmacological, and biochemical approaches together with super-resolution and live-cell microscopy, Dupraz et al. show that RhoA physiologically limits axon outgrowth by activating myosin-II-dependent actin arc formation to restrict microtubule protrusion toward the growth cone leading edge.

Dupraz et al., 2019, Current Biology *29*, 3874–3886
November 18, 2019
https://doi.org/10.1016/j.cub.2019.09.040

CellPress

CellPress

Current Biology
Article

RhoA Controls Axon Extension Independent of Specification in the Developing Brain

Sebastian Dupraz,[1] Brett J. Hilton,[1] Andreas Husch,[1] Telma E. Santos,[1] Charlotte H. Coles,[1,3] Sina Stern,[1] Cord Brakebusch,[2] and Frank Bradke[1,4,*]

[1]Axonal Growth and Regeneration Group, German Center for Neurodegenerative Diseases (DZNE), Venusberg-Campus 1, Building 99, 53127 Bonn, Germany

[2]Biotech Research & Innovation Centre, University of Copenhagen, Ole Maaløes Vej 5, 2200 Copenhagen, Denmark

[3]Present address: Immunocore, Ltd., 101 Park Drive, Milton Park, Abingdon, OX14 4RY Oxfordshire, UK

[4]Lead Contact

*Correspondence: frank.bradke@dzne.de

https://doi.org/10.1016/j.cub.2019.09.040

SUMMARY

The specification of an axon and its subsequent outgrowth are key steps during neuronal polarization, a prerequisite to wire the brain. The Rho-guanosine triphosphatase (GTPase) RhoA is believed to be a central player in these processes. However, its physiological role has remained undefined. Here, genetic loss- and gain-of-function experiments combined with time-lapse microscopy, cell culture, and *in vivo* analysis show that RhoA is not involved in axon specification but confines the initiation of neuronal polarization and axon outgrowth during development. Biochemical analysis and super-resolution microscopy together with molecular and pharmacological manipulations reveal that RhoA restrains axon growth by activating myosin-II-mediated actin arc formation in the growth cone to prevent microtubules from protruding toward the leading edge. Through this mechanism, RhoA regulates the duration of axon growth and pause phases, thus controlling the tightly timed extension of developing axons. Thereby, this work unravels physiologically relevant players coordinating actin-microtubule interactions during axon growth.

INTRODUCTION

Neurons undergo vivid morphological transitions during their development. From simple, round postmitotic cells, neurons polarize to generate subcompartments that later differentiate into sophisticated structures [1, 2]. Initial polarization is marked by axon formation [3, 4]. This process involves axon specification, singling out one among multiple neurites to become the axon and the subsequent execution of the polarity program by elongation of the specified neurite. How neurons coordinate axon specification and the execution of neuronal polarity is still unclear [5, 6].

Pioneering work identified the actin cytoskeleton as a key regulator of neuronal polarization and suggested that a dense actin network at the tip of the neurites could restrain axon formation [7–9]. Destabilization of the actin network lifts this restraint, enabling microtubules to engorge the tip of the neurites and protrude toward the growth cone leading edge, a requirement for neurite growth [7, 10–12].

It was postulated early on that the guanosine triphosphatase (GTPase) *ras homolog gene family member A* (*rhoA*) could control the stability of the actin network during neuron development [13]. RhoA is thought to promote condensation of the actin network in neurite tips acting as a negative regulator of both axon specification and axon growth [14] and therefore having a role in the establishment of neuronal polarity [5, 13, 15–19]. Consistently, molecular inactivation of RhoA induces supernumerary axons or axon growth [14, 20–23]. However, these studies are largely based on the overexpression of mutant dominant-negative (DN) and constitutively active (CA) forms of RhoA, which also scavenge guanine nucleotide exchange factors (GEFs) and GTPase-activating proteins (GAPs) of other Rho GTPases [24]. In this context, it is interesting to note that *RhoA* deletion in flies (*Drosophila melanogaster*) or mice does not result in obvious axon trajectory defects [25–28], as predicted by overexpression studies [18]. Therefore, although these studies helped to grasp the potential interactome of RhoA, the overexpression approach has limitations to resolve the actual physiological targets [24]. Hence, the physiological role of RhoA during neuronal polarization has remained unexplored [1, 2, 29].

The interplay of actin and microtubules in the growth cone likely regulates axon growth [11, 30]. Studies on the giant growth cones from stationary axons of cultured *Aplysia californica* bag neurons have provided insights into neuronal actin-microtubule interactions [10, 31, 32], which might be extendable to neurons with fast-growing axons. A characteristic cytoskeletal feature in these stationary growth cones are actin arcs, which are a dense meshwork of actin filaments reminiscent of the ventral arcs found in fibroblasts [33]. The actin motor protein myosin II [32, 34], identified as a candidate regulator of neuron polarity [19], generates these arcs by compacting actin filaments [10, 35]. Notably, in stationary *Aplysia* growth cones, actin arcs may be controlled through RhoA [36]. Actin arcs could create a barrier to hinder microtubule forward protrusion [31, 32, 35]. Hence, these structures have the potential to restrain axon growth, which makes them an attractive target for regulating axon extension. Indeed, overexpression studies showed that RhoA could regulate axon growth and that myosin II could be a potential target [19].

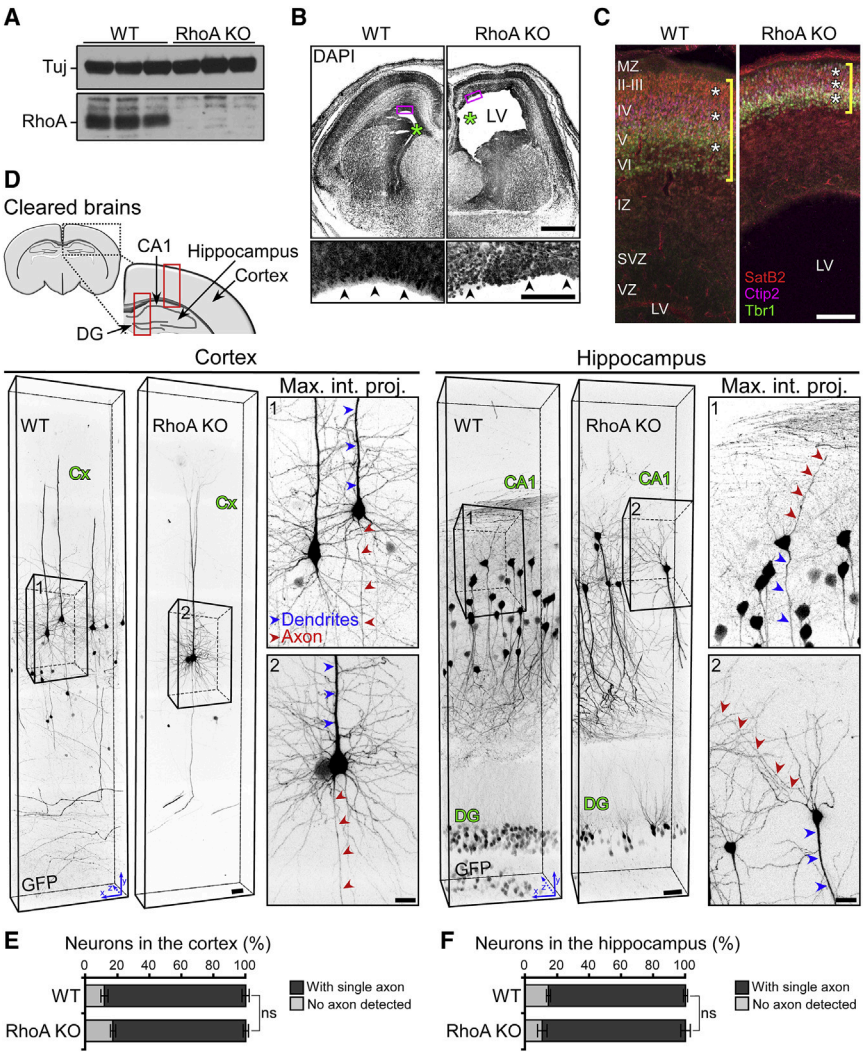

Figure 1. Establishment of Neuronal Polarity Is RhoA Independent

(A) Immunoblot of whole-brain lysates from E16.5 WT and RhoA KO embryos. Each lane represents an independent embryo brain.

(B) Automated tile scanning showing DAPI staining of WT and RhoA KO E17.5 brain coronal sections. Asterisks indicate lateral ventricles (LVs). Scale bar, 500 μm. Magnifications correspond to the frames in the main figures. Arrowheads indicate the ventricular surface. Scale bar, 100 μm.

(C) Automated tile scanning of WT and RhoA KO E17.5 brain coronal sections immunolabeled with SatB2 (red, layer II-V), Ctip-2 (magenta, layer V), and Tbr1 (green, layer VI) antibodies. White asterisks indicate the cortical layers, and yellow brackets indicate cortical plate (CP) thickness. Marginal zone (MZ), intermediate zone (IZ), subventricular zone (SVZ), and ventricular zone (VZ) are indicated. Scale bar, 100 μm.

(D) 3D reconstruction of automated multiphoton tile scanning of cleared brains from WT and RhoA KO adult mice with sparse neuronal GFP labeling. Upper diagram indicates the imaged brain areas (red rectangles), dentate gyrus (DG), and cornu ammonis 1 (CA1). Scale bars, 50 μm. Magnifications show maximum intensity projections (max. int. proj.) of the boxes in the main figures. Scale bars, 25 μm.

(E and F) Quantification of (D). Average percentage of neurons with single axons in the cortex (E) and hippocampus (F) of WT and RhoA KO brains is shown.

See also Figure S1 and Videos S1 and S2. Values are plotted as mean ± SEM; ns, not significant by Student's t test. WT, N = 290; RhoA KO, N = 176 neurons from n = 7 and n = 6 cortices, respectively; WT, N = 91; RhoA KO, N = 125 neurons from n = 4 and n = 5 hippocampi, respectively.

Here, using genetic deletion experiments followed by *in vivo* and cell culture analysis in combination with time-lapse and high-resolution microscopy, we demonstrate that axon specification is independent of RhoA. However, RhoA regulates the onset and timing of neuronal polarization. Specifically, we show that RhoA, by controlling microtubule protrusion into the growth cone periphery through myosin-II-generated actin arcs, instructs the duration of growth and pause phases that dictate the speed of axon outgrowth.

RESULTS

RhoA Regulates Neuronal Polarization by Restraining Axon Initiation and Growth, but Not Axon Specification

To assess the physiological function of RhoA during neuronal polarization, i.e., axon specification, axon initiation, and axon growth, we generated mice with conditional CNS-targeted deletion of RhoA (*nestin-cre*$^{tg/-}$, *RhoA*$^{fl/fl}$; termed hereafter RhoA KO). Immunoblot analysis showed that the RhoA protein was undetectable in brain extracts from embryonic day (E)16 RhoA KO embryos (Figure 1A). RhoA KO brains had several abnormalities compared to brains from control littermates, including enlarged ventricles with uneven cellular organization at their surface (Figure 1B) accompanied by a thin cortical plate (CP) and compacted lamination (Figure 1C).

To investigate the involvement of RhoA in axon specification, we tested whether neurons in RhoA KO brains contained supernumerary axons. To characterize the three-dimensional morphology of RhoA KO neurons, we cleared adult brains of RhoA KO mice that were crossed with the GFP-M mouse line, in which neurons are sparsely labeled throughout the brain (*nestin-cre*$^{tg/-}$, *RhoA*$^{fl/fl}$, *gfp-m*$^{tg/-}$; termed hereafter RhoA KO[GFP]) [37, 38]. Two-photon microscopy of the cleared cortex and hippocampus showed that RhoA KO [GFP] neurons feature only a single axon emanating from their cell body, as found in neurons from control WT[GFP] mice (*nestin-cre*$^{-/-}$, *RhoA*$^{fl/fl}$, *gfp-m*$^{tg/-}$; Figures 1D–1F; Videos S1 and S2).

The possibility remained that, in the absence of RhoA, neurons would form supernumerary axons early during development that would be pruned at a later time point. To test this, we electroporated the brains of *RhoA*$^{fl/fl}$ embryos *in utero* with a plasmid

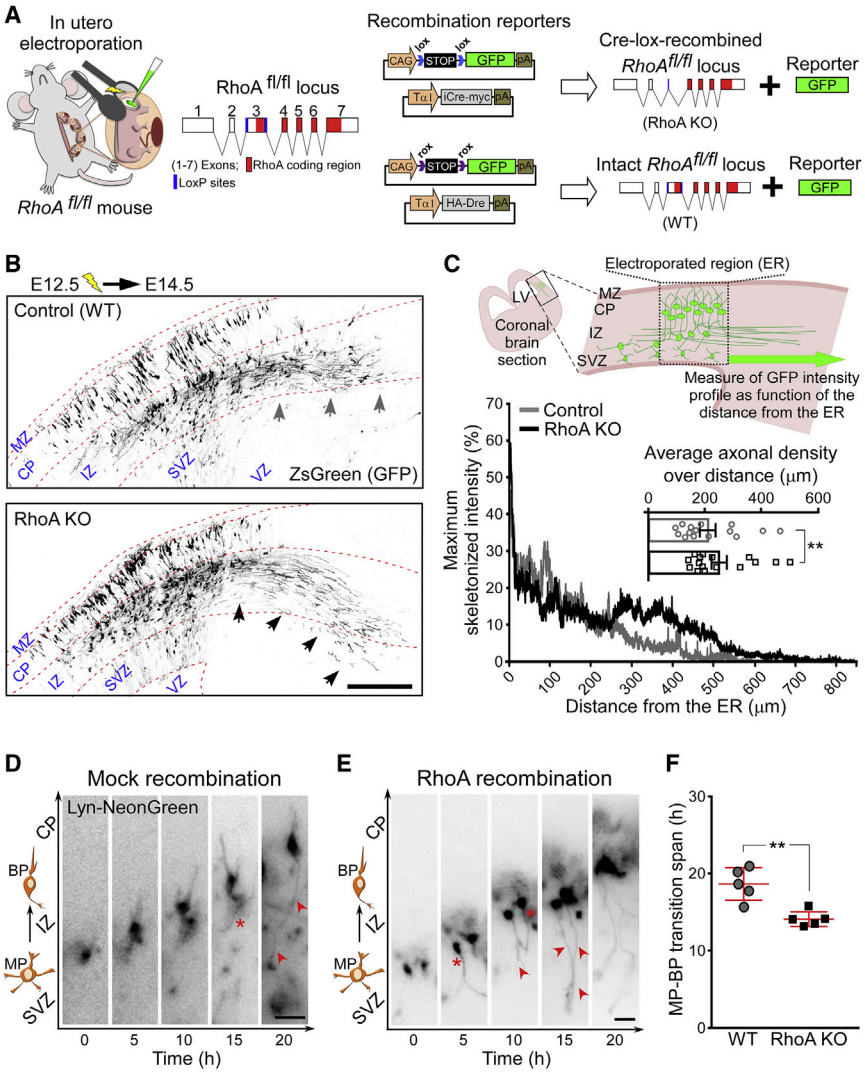

Figure 2. Neuron-Specific RhoA Deletion *In Vivo* Accelerates Neuronal Polarization

(A) Scheme illustrating the plasmid pairs used for *in utero* and *ex utero* electroporations. GFP is ZsGreen (A and B; Figure S2A) or Lyn-NeonGreen (D and E).

(B) Automated confocal tile scanning of coronal sections from E14.5 *RhoA*$^{fl/fl}$ brains electroporated *in utero* at E12.5. Grey and black arrows indicate axons from WT and RhoA KO neurons, respectively. Scale bar, 200 μm.

(C) Quantification of (B). Upper diagram depicts the analysis. The gray (WT) and black (RhoA KO) curves represent the average density of axons extending from the electroporated region (ER). The bar plot indicates the average axonal density over distance from the ER. Each dot represents the average of two consecutive slices from a single brain. Values are plotted as mean ± SEM; **p < 0.01 by a customized ANOVA test (F-test). WT; N = 14 and RhoA KO; N = 15 sections from n = 7 electroporated brains each.

(D and E) Representative time-lapse images of GFP positive WT (D) and RhoA KO (E) cortical neurons in cultured coronal sections from brains electroporated at E13.5. Asterisks indicate the beginning of the bipolar (BP) stage and arrowheads the emergent trailing process (nascent axon, arrowheads). Scale bars, 25 μm.

(F) Quantifications of (D) and (E). The duration of the MP-BP transition for WT and RhoA KO neurons is plotted as mean ± SEM; **p < 0.01 by Student's t test. WT, N = 222 neurons and RhoA KO, N = 317 neurons from n = 5 independent electroporated brains each.

See also Figures S1 and S2A and Video S3.

encoding Cre recombinase under the control of the neuron-specific tubulin-alpha-1 promoter (pTα1-Cre) together with a loxP GFP (Zoanthus sp. (Zs)Green)-based recombination reporter plasmid (Figure 2A). Thereby, recombination only occurs in neurons. Hence, the generated RhoA KO neurons develop in a wild-type (WT)-like environment. As a control, we electroporated a plasmid encoding Dre integrase driven by the same Tα1 promoter (pTα1-Dre) together with a roxP GFP (ZsGreen)-based reporter plasmid, leading to MOCK recombination (Figure 2A). Cre recombinase-mediated deletion of RhoA by electroporation at E13.5 led to more rapid neuronal migration (Figures S1A and S1B), confirming previous results [28], and the near absence of RhoA in biochemical extracts of *RhoA*$^{fl/fl}$ cortical neurons within 1 day *in vitro* (DIV) (Figure S1C). Importantly, neuronal polarization was not affected. RhoA KO and WT neurons in the CP of E15.5 electroporated brains displayed a typical polarized bipolar (BP) morphology (83.3% ± 1.1% versus 85.1% ± 2.1%, respectively; p = 0.52; Figure S1D) characterized by one leading process and a single trailing process, which will later become the axon (Figure S1E) [39]. Hence, axon specification is independent of RhoA.

Next, we investigated the role of RhoA in axon initiation and growth. To analyze early axon formation *in vivo*, we electroporated *RhoA*$^{fl/fl}$ embryos at E12.5, allowing axons from recombined neurons to elongate as pioneer axons [3], and analyzed their trajectories at E14.5. Although axons from both RhoA KO and control neurons emerged within the CP and intermediate zone (IZ) (Figures 2B and 2C), RhoA KO axons covered longer distances than control axons (Figures 2C and S2A). To assess the dynamics of initial axon outgrowth, we prepared organotypic slice cultures from E13.5 *ex utero* electroporated (EUE) embryos and performed live-cell imaging 1 day later. RhoA KO neurons transitioned quicker from the multipolar (MP) to the bipolar (BP) stage and developed their single axon faster than WT neurons (14.1 h ± 0.4 h versus 18.6 h ± 0.9 h, respectively; p < 0.01; Figures 2D–2F; Video S3).

Dissociated RhoA KO hippocampal neurons recapitulated the *in vivo* phenotype and showed a more rapid polarization (Figures 3A and 3B). As early as 12 h after plating, more than twice as many RhoA KO neurons contained an axon positive for the axonal marker Tau-1 compared to WT control neurons (Figure 3C; 39.5% ± 4.3% versus 16.9% ± 4.5%, respectively; p < 0.0001). Axons of RhoA KO neurons were also longer than those generated by WT neurons (Figure 3D). At later time points, WT

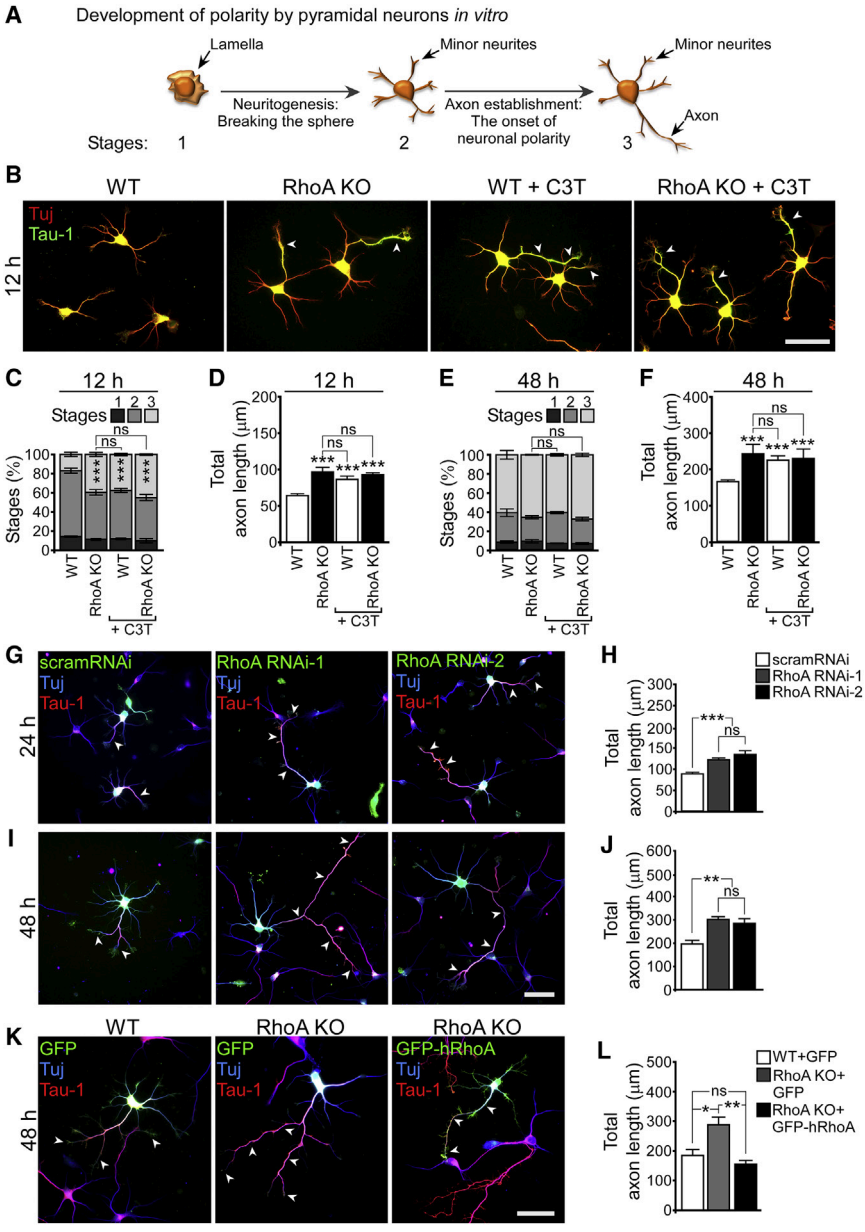

Figure 3. RhoA Restrains Neuronal Polarization and Axon Growth

(A) Scheme illustrating the development of cultured pyramidal neurons.

(B) Representative fluorescence images of dissociated E17.5 WT and RhoA KO hippocampal neurons cultured for 12 h with or without C3T treatment. Immunolabeling for βIII tubulin (Tuj, red) and Tau-1 (green) is shown. Arrowheads indicate Tau-1-positive axons. Scale bar, 50 μm.

(C and D) Quantification of (B).

(C) Average percentage of neurons in stages 1–3.

(D) Average total length of Tau-1-positive axons. WT, N = 266; RhoA KO, N = 306; WT+C3T, N = 321; and RhoA KO+C3T, N = 286 neurons from n = 4 independent experiments.

(E and F) Morphological assessment of dissociated hippocampal neurons cultured 48 h in the same conditions as in (B).

(E) Average percentage of neurons in stages 1–3.

(F) Average total length of Tau-1-positive axons. WT, N = 439; RhoA KO, N = 316; WT+C3T, N = 376; and RhoA KO+C3T, N = 335 neurons from n = 4 independent experiments.

(G) Representative fluorescence images of dissociated E17.5 hippocampal neurons electroporated with a mix of GFP-expressing reporter plasmids plus either scrambled RNAi (scramRNAi), RhoA RNAi-1, or RhoA RNAi-2 and cultured for 24 h. Immunolabeling for βIII tubulin (Tuj, blue) and Tau-1 (red) is shown. Arrowheads indicate Tau-1-positive axons. Scale bar, 50 μm.

(H) Quantification of (G). Average total length of Tau-positive axons is shown. scramRNAi, N = 139; RhoA-RNAi-1, N = 119; and RhoA-RNAi-2, N = 143 neurons from n = 3 independent experiments.

(I) Representative fluorescence images of 48-h cultures of dissociated E17.5 hippocampal neurons electroporated and immunolabeled as in (G). Arrowheads indicate Tau-1-positive axons. Scale bar, 50 μm.

(J) Quantification of (I). Average total length of Tau-positive axons is shown. scramRNAi, N = 115; RhoA-RNAi-1, N = 121; and RhoA-RNAi-2, N = 94 neurons from n = 3 independent experiments.

(K) Representative fluorescence images of 48-h cultures of WT and RhoA KO hippocampal neurons expressing GFP (left and middle, respectively) and RhoA KO hippocampal neurons expressing GFP-hRhoA (right). Immunolabeling for βIII tubulin (Tuj, blue) and Tau-1 (red) is shown. Arrowheads indicate Tau-1-positive axons. Scale bar, 50 μm.

(L) Quantification of (K). Average total length of Tau-positive axons is shown. WT+GFP, N = 140; RhoA KO+GFP, N = 121; and RhoA KO+GFP-hRhoA, N = 95 neurons from n = 3 independent experiments.

See also Figures S2G, S2H, and S3A–S3D. Values are plotted as mean ± SEM (C and E) or mean + SEM (D, F, H, J, and L). Statistical significance: ***p < 0.001; **p < 0.01; *p < 0.05; ns, not significant by ordinal logistic regression (C and E; see Statistical Analysis section), by generalized linear model test (D and F; see Statistical Analysis section), and by one-way ANOVA followed by Tukey's post-test (H, J, and L).

neurons also formed an axon (Figure 3E), but axons of RhoA KO neurons continued to be substantially longer (Figure 3F). Interestingly, in RhoA KO neurons, the onset of spontaneous excitatory postsynaptic currents (sEPSCs) was detected earlier compared to WT neurons, suggesting an acceleration of synaptic maturation. Already at 4 DIV, 13.3% (4 out of 30) of RhoA KO neurons showed sEPSCs, which were not detected in WT neurons (0 out of 29; Figures S2B and S2C). After 7 DIV, 85% (17 out of 20) of cultured RhoA KO neurons showed sEPSCs compared to only 38.9% (7 out of 18) of WT neurons (Figures S2B and S2C). Moreover, RhoA KO neurons showed a higher frequency of sEPSCs than WT neurons (RhoA KO, 2.2 ± 0.8 Hz versus WT, 0.2 ± 0.1 Hz; p < 0.001; Figure S2D), while the amplitudes of the sEPSCs were similar between WT and RhoA KO neurons (96.2 ± 30.5 pA versus RhoA KO, 81.4 ± 10.3 pA, respectively; p = 0.74; Figure S2E).

Acute downregulation of RhoA by two independent RNAi probes mirrored the RhoA KO phenotype (Figures 3G–3J and

S2F). Re-expression of RhoA in RhoA KO neurons restored a shorter axon equal to WT neurons (Figures 3K and 3L). Consistent with our *in vivo* results, we did not observe differences in the number of neurons bearing multiple axons between WT and RhoA KO cultures (2.9% ± 1.3% versus 4.0% ± 1.0%, respectively; $p = 0.52$; Figure S2G). Interestingly, WT neurons treated with C3 exoenzyme, which inactivates all RhoA, RhoB, and RhoC [40], showed a growth pattern indistinguishable from RhoA KO neurons, suggesting a prominent role for RhoA at this stage of axon development (Figures 3B–3F). Notably, additional inactivation of RhoB and RhoC by C3 exoenzyme in RhoA KO neurons did not increase the number of neurons containing multiple axons (RhoA KO versus RhoA KO+C3T; 4.0% ± 1.0% versus 6.5% ± 1.3%, respectively; $p = 0.09$; Figure S2G) or affect axon length (Figures 3B–3F). Similarly, downregulation of RhoB by an RNAi approach in RhoA KO neurons (Figure S3A) neither enhances axon growth further (Figures S3B and S3C) nor generates additional neurons with supernumerary axons (Figure S3D) compared to RhoA KO neurons. Thus, although RhoA is not involved in axon specification, it restrains the onset and rate of neuronal polarization.

Non-muscular Myosin II Is a Physiological Target of RhoA during Neuronal Polarization

To determine the physiologically relevant effectors downstream of RhoA that restrain axon growth, we first assessed RhoA crosstalk with other related Rho-GTPases. Cdc42 and Rac1 are known promoters of axon growth whose genetic ablation severely impairs axon outgrowth [41, 42]. We examined the protein level and activation state of Cdc42 and Rac1 in biochemical extracts of cultured cortical RhoA KO neurons and found them to be similar to WT neurons (Figures S3E–S3G). RhoA activates *Rho*-associated, coiled-coil-containing protein kinase (ROCK) as its immediate downstream target [43] (Figure 4A). Consistently, in biochemical extracts from cultured cortical RhoA KO neurons, ROCK activity decreased compared to WT extracts (Figure 4B). Overexpression studies in cell lines have previously shown that activated ROCK phosphorylates LIM domain kinase (LIMK) [44, 45], which in turn regulates cofilin activity [46, 47] (Figure 4A). Moreover, cofilin drives neurite formation [48] and axon regeneration in the CNS [49]. However, immunoblot analysis of extracts from cortical neuronal cultures revealed no difference in the level of phosphorylated (p)-LIMK or of p-cofilin between WT and RhoA KO neurons (Figures 4C–4F). Immunocytochemistry confirmed that the p-cofilin/cofilin ratio in the growth cone was similar between WT and RhoA KO hippocampal neurons (Figures 4G and 4H), further suggesting that RhoA does not regulate axon growth through cofilin.

ROCK also activates myosin II by directly phosphorylating its regulatory myosin light chain (MLC2) and also indirectly by phosphorylation of the regulatory myosin phosphatase target subunit-1 (MYPT-1) of the myosin phosphatase [50, 51] (Figure 4A). Indeed, immunoblot analysis of cultured cortical neuronal extracts and immunocytochemistry showed that both p-MYPT-1 and p-MLC2 levels decreased in RhoA KO compared to WT hippocampal neurons (Figures 4I–4N). Hence, myosin-II-actin-mediated restraint could be a potential physiological regulator of axon growth downstream of RhoA.

Myosin II Restrains Axon Growth Downstream of RhoA

Inactivation of myosin II in hippocampal WT neurons by using 20 μM blebbistatin (Blebb) leads to the generation of supernumerary axons (Figure S3H), consistent with previous reports [23, 52]. As myosin II was only partially inactivated in RhoA KO neurons, we asked whether a moderate decrease in myosin II activity could recapitulate the RhoA KO phenotype by enhancing onset and rate of neuronal polarization without perturbing axon specification. WT hippocampal neurons treated with 0.5 μM Blebb fully recapitulated the phenotype of RhoA KO neurons at all observed time points (Figures 5A–5E and S3I). Already at 12 h, Blebb-treated cultures showed a higher proportion of stage 3 neurons and longer axons compared to control WT neurons (Figures 5A–5C). Moreover, at later time points, Blebb-treated neurons had extended a long axon without forming supernumerary axons, preserving neuronal polarity (Figures 5D, 5E, and S3I). Time-lapse microscopy revealed that axons of hippocampal RhoA KO neurons and Blebb-treated WT neurons grew not only faster than axons from vehicle-treated WT neurons (Figures 5F and 5G; Video S4) but also paused for shorter periods of time (1.67 h ± 0.06 h and 1.48 h ± 0.12 h versus 2.07 h ± 0.09 h, respectively; $p < 0.01$; Figures 5H and S3J). Conversely, overexpression of a phospho-mimetic (T18D; S19D) constitutively active MLC2 mutant (MLC2-CA) in RhoA KO neurons abolished their characteristic early-polarity onset and drastically reduced axonal growth (Figures S5A–S5F).

We asked next whether the growth enhancement found after myosin II inhibition could be recapitulated by actin destabilization. Indeed, similar to myosin II inhibition, destabilizing the actin cytoskeleton with high latrunculin A (Lat A) doses (25 nM) led to the formation of supernumerary axons (Figures S3H and S4A), while modest Lat A doses (5 nM) accelerated the onset of axon initiation and enhanced the growth of a single axon, hence maintaining polarity (Figures S4A–S4D). Thus, mild actin instability caused by partial inhibition of myosin II activity drives the enhanced axon growth of developing RhoA KO neurons.

RhoA Drives Actin Arc Formation in the Growth Cone through Myosin II

As the machinery for axon growth is thought to be located in its growth cone, we characterized the growth cone cytoskeleton in RhoA KO neurons. Phalloidin staining of fixed co-cultures of WT and RhoA KO hippocampal neurons (Figure S6A) revealed a comparable amount and a similar distribution of polymerized fibrous (F)-actin between WT and RhoA KO neurons (Figure 6A). The balance between soluble globular (G) actin and F-actin has previously been proposed to be an indicator of gross changes in growth cone cytoskeleton dynamics and axon growth [48]. An equal G/F-actin ratio was found between biochemical extracts from WT and RhoA KO neuronal cultures (Figures 6B and 6C). Importantly, however, stimulated emission depletion (STED) microscopy revealed structural differences in growth cone actin architectures. Although the majority (83.3% ± 0.9%) of WT neurons contained actin arcs in their axonal growth cone, these structures were present in few RhoA KO growth cones (23.2% ± 0.5%; $p < 0.0001$; Figures 6D and 6E). Moreover, F-actin bundles in WT growth cones were prominent at the peripheral (P)-domain of the growth cone and terminated within the actin arc structures at the transition (T)-domain. In RhoA

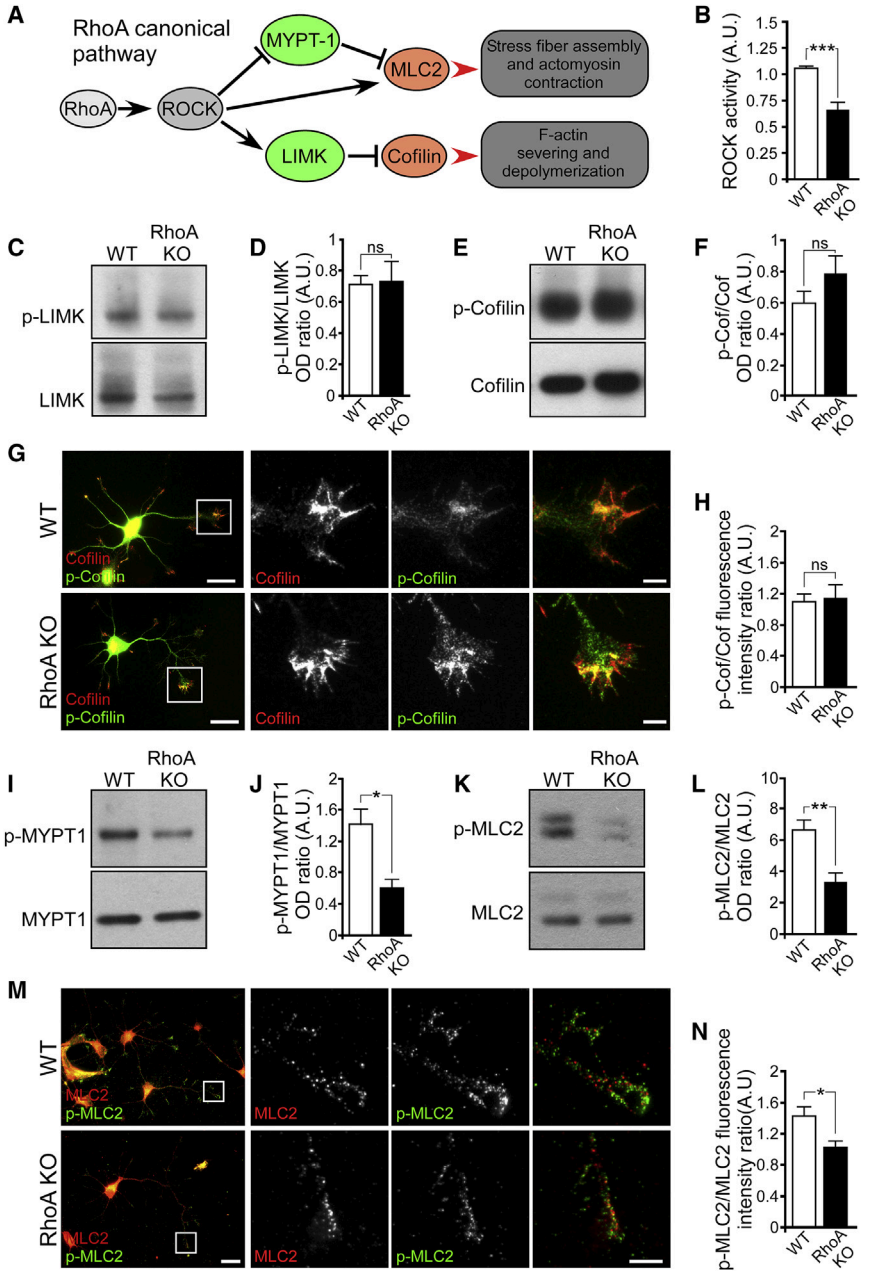

Figure 4. RhoA Regulates Cytoskeleton Organization and Dynamics through Myosin II and Independent of Cofilin

(A) Schematic of RhoA canonical signaling and its effects on actin structures.

(B) Quantification of ROCK activity in cultured neurons. WT, N = 5 and RhoA KO, N = 6 lysates from n = 3 independent experiments.

(C) Immunoblot showing protein levels for phospho(p)-LIMK and total LIMK in cell lysates from cultured WT and RhoA KO neurons.

(D) Quantification of (C). WT, N = 4 and RhoA KO, N = 4 lysates from n = 4 independent experiments.

(E) Immunoblot showing protein levels for phospho(p)-cofilin and total cofilin in cell lysates from cultured WT and RhoA KO neurons.

(F) Quantification of (E). WT, N = 4 and RhoA KO, N = 4 lysates from n = 4 independent experiments.

(G) Representative fluorescence images of 24-h cultures of WT (upper row) and RhoA KO (lower row) neurons immunolabeled for total cofilin (red) and p-cofilin (green). Scale bars, 25 μm. Magnified insets show the axonal growth cone. Scale bars, 5 μm.

(H) Quantification of (G). WT, N = 37 and RhoA KO, N = 41 axonal growth cones from n = 4 independent experiments.

(I) Immunoblot showing protein levels for phospho(p)-MYPT1 and total MYPT1 in cell lysates from cultured WT and RhoA KO neurons.

(J) Quantification of (I). WT, N = 3 and RhoA KO, N = 3 from n = 3 independent experiments.

(K) Immunoblot showing protein levels for phospho(p)-MLC2 and total MLC2 in cell lysates from cultured WT and RhoA KO neurons.

(L) Quantification of (K). WT, N = 5 and RhoA KO, N = 5 from n = 5 independent experiments.

(M) Representative fluorescence images of 24-h cultures of WT (upper row) and RhoA KO (lower row) neurons immunolabeled for total MLC2 (red) and p-MLC2 (green). Scale bar represents 25 μm. Magnified insets show the axonal growth cone. Scale bar, 5 μm.

(N) Quantification of (M). WT, N = 40 and RhoA KO, N = 39 axonal growth cones from n = 4 independent experiments.

See also Figures S3E–S3G. All values are plotted as mean + SEM. Statistical significance: ***p < 0.001; **p < 0.01; *p < 0.05; ns, not significant by Student's t test.

KO growth cones, by contrast, F-actin bundles were longer and many spanned from the leading edge to the base of the growth cone (Figures 6D and 6F).

Pharmacological myosin II inactivation reproduced the RhoA KO growth cone morphology. WT hippocampal neurons treated with 0.5 μM Blebb lacked actin arcs in their growth cones (30.8% ± 0.9% versus 83.3% ± 0.9% for Blebb versus WT, respectively; $p < 0.01$), similar to the decrease detected in growth cones of RhoA KO neurons (Figures 6D and 6E). Moreover, the F-actin bundles of Blebb-treated WT growth cones were longer compared to the F-actin bundles of WT growth cones but similar to those of RhoA KO growth cones (Figures 6D and 6F). Conversely, overexpression of constitutively active form (MLC2-CA) in RhoA KO neurons restored actin arc formation to WT-like levels (Figures S5G and S5H). Thus, RhoA generates actin arcs in the growth cone through myosin II.

Myosin-II-Generated Actin Arcs Downstream of RhoA Impede Axon Growth by Restraining Microtubule Protrusion

In growth cones of mouse pyramidal neurons (Figure S6B), actin retrograde flow speed decreases at the T-domain, relative to the P-domain, as actin filaments become compressed against the actin arcs, recapitulating processes of stationary *Aplysia* growth cones [10]. Given the loss of actin arcs and the extension of F-actin bundles into the central (C)-domain in RhoA KO growth

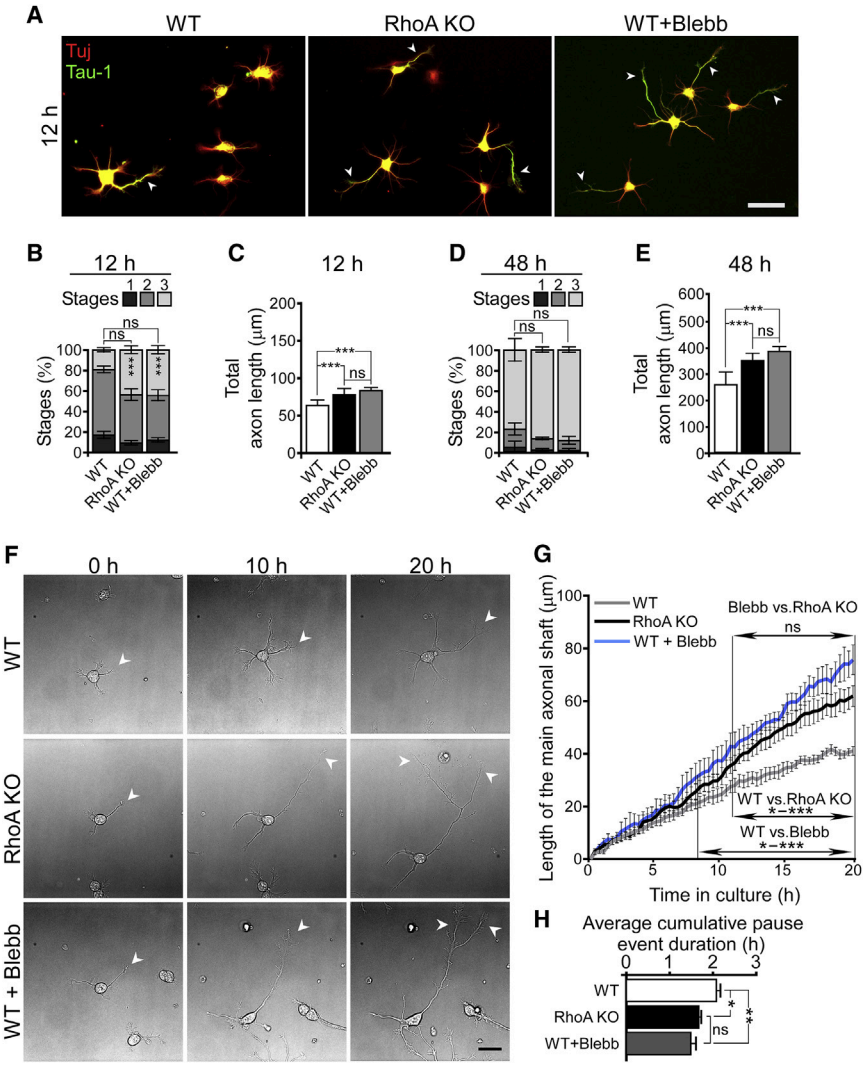

Figure 5. Partial Myosin II Inhibition Recapitulates the Accelerated Onset of Polarity and Enhanced Axonal Growth of RhoA KO Neurons

(A) Representative fluorescence images of dissociated E17.5 hippocampal WT, RhoA KO, and 0.5 μM-Blebb-treated WT neurons after 12 h in culture. Immunolabeling for βIII tubulin (Tuj, red) and Tau-1 (green) is shown. Arrowheads indicate Tau-1-positive axons. Scale bar, 50 μm.

(B and C) Quantification of (A).

(B) Average percentage of neurons in stages 1–3.

(C) Average total length of Tau-1-positive axons. WT, N = 278; RhoA KO, N = 281; and WT+Blebb, N = 271 neurons from n = 3 independent experiments.

(D and E) Morphological assessment of dissociated hippocampal neurons cultured 48 h in the same conditions as in (A).

(D) Average percentage of neurons in stages 1–3.

(E) Average total length of Tau-1-positive axons. WT, N = 159; RhoA KO, N = 157; and WT+Blebb, N = 136 neurons from n = 3 independent experiments.

(F) Representative bright-field micrographs from a 20-h time-lapse video microscopy of WT (upper row), RhoA KO (middle row), and 0.5 μM-Blebb-treated (bottom row) neurons growing in culture. White arrowheads indicate the axon. Scale bar, 25 μm.

(G) Average axon elongation (primary shaft) over time for the neurons in (F). WT, N = 32; RhoA KO, N = 40; and WT+Blebb, N = 23 neurons from n = 4 independent experiments.

(H) Average cumulative duration of axon pause events for the neurons in (G). The number of cells analyzed is the same as in (G).

See also Figures S3H–S3J, S4A–S4D, and S5 and Video S4. Values are plotted as mean ± SEM (B, D, and G) or mean + SEM (C, E, and H). Statistical significance: ***p < 0.001; **p < 0.01; *p < 0.05; ns, not significant by ordinal logistic regression (B and D; see Statistical Analysis section), by generalized linear model test (C and E; see Statistical Analysis section), and by one-way ANOVA followed by Tukey's post-test (G and H).

cones, we hypothesized that centripetal movement of actin filaments might therefore be unrestricted and turnover more rapidly. Indeed, time-lapse imaging of actin dynamics in growth cones from hippocampal RhoA KO neurons transfected with Lifeact [53] (Figure 7A) showed increased retrograde flow compared to WT growth cones (Figure 7B). Myosin II inactivation recapitulated the RhoA KO phenotype: actin retrograde flow in the P-domain of the growth cone was enhanced in Blebb-treated WT neurons, reaching speeds comparable to RhoA KO neurons (Figure 7B). Moreover, the speed of actin retrograde flow in the T-domain of growth cones of RhoA KO neurons was significantly higher than the actin retrograde flow measured in WT neurons but similar to Blebb-treated WT neurons (6.02 ± 0.14 μm/min versus 5.92 ± 0.12 μm/min versus 5.52 ± 0.12 μm/min, respectively; WT versus RhoA KO $p < 0.05$; WT versus Blebb $p < 0.05$; RhoA KO versus Blebb $p = 0.59$; Figure 7B, right). This finding raises the possibility that increased actin retrograde flow in the growth cone T-domain reflects the disassembly of the actin arc barrier, which might lead to a less-efficient retention of microtubules in the C-domain.

We therefore studied microtubule advance in neurons expressing end-binding protein 3 (EB-3), a marker of polymerizing microtubule ends, fused to mCherry [48, 54] (Figure 7C). In both RhoA KO and Blebb-treated WT growth cones, we found that microtubule advance speed in the P-domain was higher compared to WT growth cones (Figure 7D). As a result, microtubules reached closer to the leading edge of RhoA KO and Blebb-treated WT growth cones compared to vehicle-treated WT growth cones (Figures 6D, 7C, and 7E; Video S5). Similarly, growth cones of fast-elongating Lat-A-treated axons showed a disorganized actin network without actin arcs (Figures S4E–S4G). This, in turn, led microtubules to reach closer to the growth cone leading edge compared to the microtubules in vehicle-treated growth cones (Figures S4E and S4H–S4J). These findings further support the hypothesis that RhoA impedes axon growth by restraining microtubule protrusion into the P-domain of the growth cone. To test this hypothesis directly, we deduced that moderate microtubule destabilization should reverse the enhanced axon growth observed in RhoA KO neurons. Indeed, cultured RhoA KO neurons with low doses of the

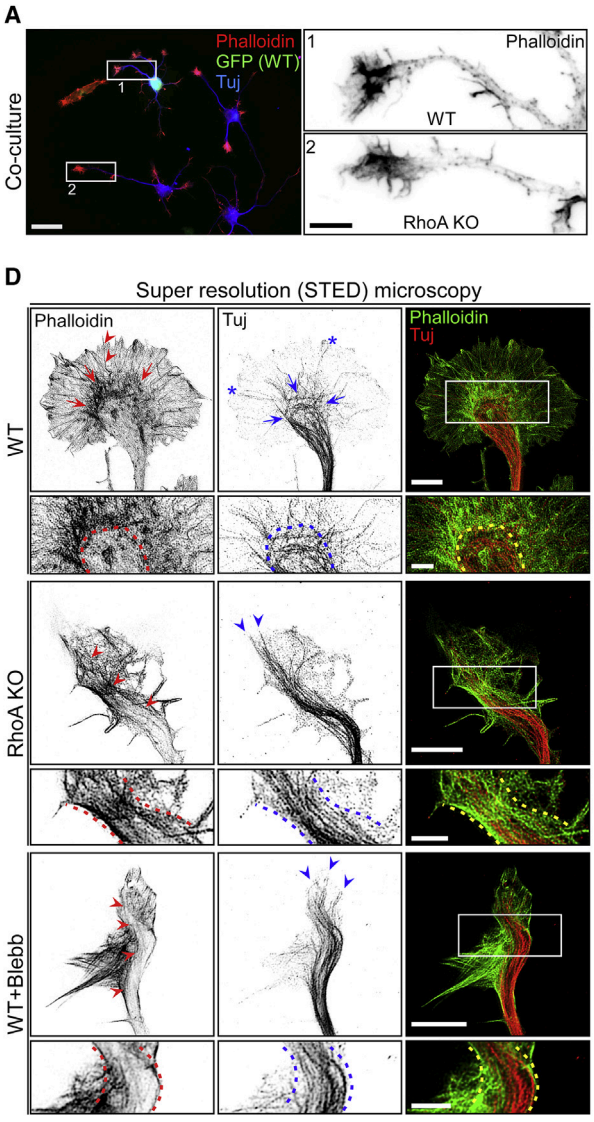

Figure 6. Partial Myosin II Inhibition in WT Neurons Leads to Actin and Microtubule Cytoskeleton Rearrangements, which Mimic that of RhoA KO Neurons

(A) Representative fluorescence images of dissociated WT (GFP positive) and RhoA KO E17.5 hippocampal neurons co-cultured for 12 h. Immunolabeling for βIII tubulin (Tuj, blue) and phalloidin (F-actin, red) is shown. Scale bar, 25 μm. Magnifications (right) feature phalloidin staining of the growth cones boxed in the main figure. Scale bar, 5 μm.

(B) Immunoblot shows the levels of G-actin and F-actin in cell lysates from cultured WT and RhoA KO neurons.

(C) Quantification of (B). WT, N = 6 and RhoA KO, N = 5 lysates of cultured neurons from n = 3 independent experiments.

(D) Super-resolution micrographs of axonal growth cones from WT (upper row), RhoA KO (middle row), and 0.5-μM-Blebb-treated (bottom row) neurons. Immunolabeling for βIII tubulin (Tuj, red) and phalloidin (F-actin, green) is shown. Red arrows indicate actin arc-rich T-domain and red arrowheads F-actin bundles. Microtubules in the growth cone P-domain are indicated by blue asterisks, bundled microtubules by blue arrowheads, and microtubules retained in the C-domain by blue arrows. Scale bars, 5 μm. Magnifications correspond to the frames in the main figures. Dashed lines in the magnifications represent the alignment of F-actin (red) with respect to microtubules (blue). Scale bars, 2 μm.

(E) Quantification of (D). Average percentage of axonal growth cones featuring actin arcs is shown. WT, N = 48; RhoA KO, N = 56; and WT+Blebb, N = 52 growth cones from n = 5 independent experiments.

(F) Quantification of (D). Average length of F-actin bundles in axonal growth cones is shown. WT, N = 38; RhoA KO, N = 42; and WT+Blebb, N = 31 growth cones from n = 4 independent experiments.

See also Figures S4E–S4H, S5G–S5H, S6A, and S7A and Videos S5 and S6. Values are plotted as mean ± SEM (C and E) or mean + SEM (F). Statistical significance: ***p < 0.001; **p < 0.01; *p < 0.05; ns, not significant by Student's t test (C) and one-way ANOVA followed by Tukey's post-test (E and F).

microtubule-destabilizing drug nocodazole (50 nM) decreased their axonal lengths to measurements found in WT control neurons (Figures 7F and 7G). Hence, modest microtubule destabilization in RhoA KO neurons restores WT-like neuronal morphology. Thus, RhoA restrains axon growth by confining microtubules to the central growth cone domain through myosin-II-generated actin arcs (Figure S7A).

DISCUSSION

Polarization is a hallmark of neuronal development. It involves the specification of the future axon from several minor neurites and the execution of a growth program in the specified neurite through accelerated growth. Here, we demonstrate that RhoA is not required for axon specification, but it decelerates neuronal polarization in the developing mammalian brain. RhoA restrains neuronal polarization and axon growth by inducing myosin-II-generated actin arcs to prevent microtubule protrusion in the axonal growth cone. We will discuss in detail how these findings change our perspective on neuronal polarization.

The Physiological Role of RhoA during Neuronal Polarization

The Rho-GTPases Cdc42 and Rac1 cause actin rearrangements that favor neurite outgrowth and axon formation [9, 41, 42, 55], whereas high RhoA activity was thought to prevent minor neurites from becoming axons [1, 5, 16, 56, 57]. Strikingly, our data demonstrate that RhoA is not involved in axon specification. RhoA KO neurons achieved the prototypical polarized architecture: they contained a single axon and multiple dendrites both in culture and *in vivo* during development, as well as in the adult brain. Instead, RhoA is involved in the onset and timing of neuronal polarity. Our analyses of RhoA KO neurons in the developing brain as well as in cell culture pinpoints RhoA as a

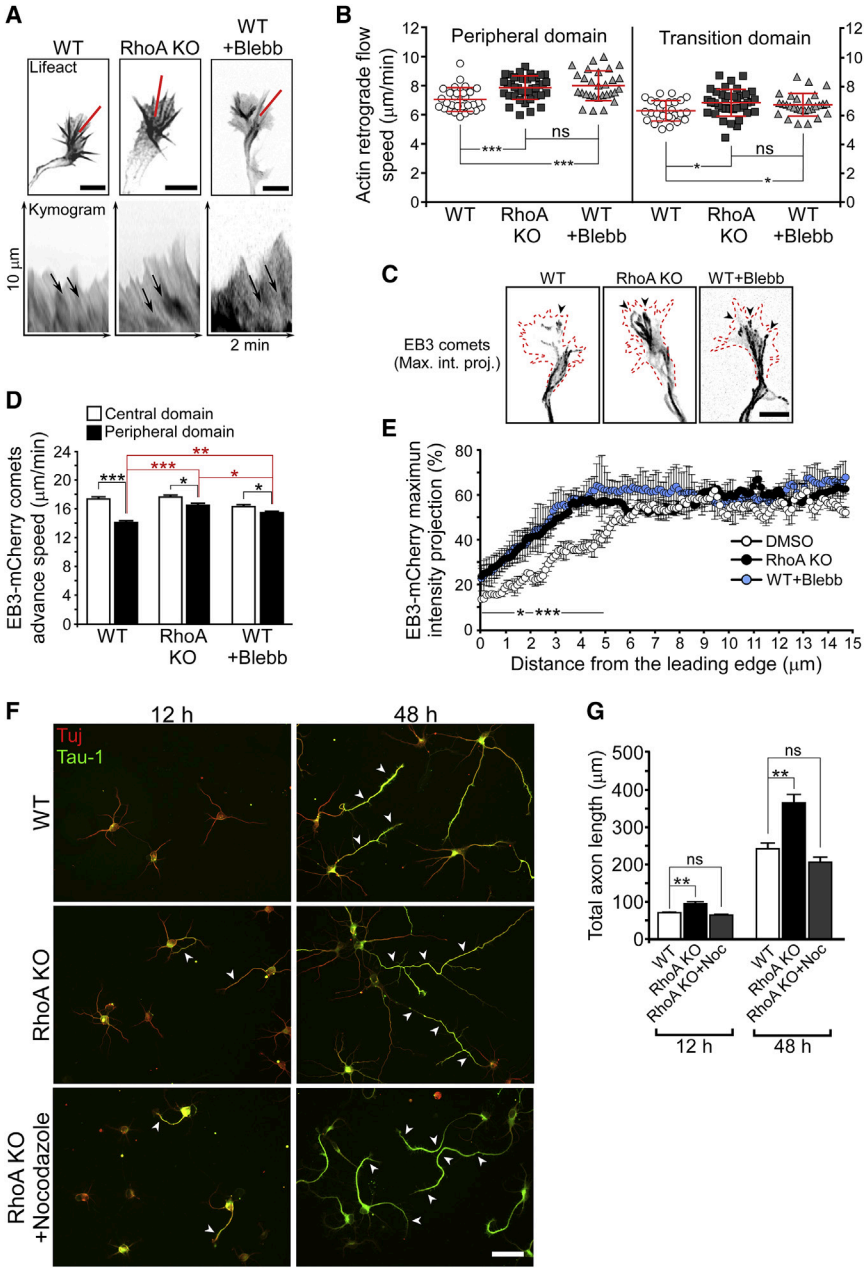

Figure 7. Partial Myosin II Inhibition Is Sufficient to Reproduce the Dynamics of RhoA KO Neurons

(A) Representative construction of kymographs from axonal growth cones of E17.5 hippocampal neurons expressing Lifeact-GFP. Line scans used to create the kymographs are shown in red. Black arrows correspond with actin retrograde flow speed. Scale bars, 5 μm.

(B) Average speed of actin retrograde flow in the P-domain (left) and T-domain (right) in axonal growth cones. WT, N = 29; RhoA KO, N = 39; and WT+Blebb, N = 29 axonal growth cones from n = 3 independent experiments.

(C) Maximum intensity projection (max. int. proj.) of time-lapse image series taken from axonal growth cones from hippocampal neurons expressing EB3-mCherry in the different conditions. Arrowheads indicate microtubules that reached the leading edge (red dashed line). Scale bar, 5 μm.

(D) Average advance speed of EB3-mCherry comets. WT, N = 24; RhoA KO, N = 24; and WT+Blebb, N = 26 axonal growth cones from n = 3 independent experiments.

(E) Average percentage intensity of EB3-mCherry signal with respect to the growth cone leading edge. WT, N = 28; RhoA KO, N = 37; and WT+Blebb, N = 29 axonal growth cones from n = 3 independent experiments.

(F) Representative fluorescence images of dissociated E17.5 hippocampal neurons after 12 and 48 h in culture. From top to bottom: WT, RhoA KO, and RhoA KO plus nocodazole treatment is shown. Immunolabeling for βIII tubulin (Tuj, red) and Tau-1 (green) is shown. Arrowheads indicate axons. Scale bar, 50 μm.

(G) Quantification of (F). Average total length of tau-positive axons. 12 h: WT, N = 373; RhoA KO, N = 425; and RhoA KO+nocodazole, N = 351; 48 h: WT, N = 321; RhoA KO, N = 303; and RhoA KO+nocodazole, N = 312 neurons from n = 4 independent experiments.

See also Figures S4I, S4J, S6B, and S7A and Videos S5 and S6. Values are plotted as mean ± SEM (B and E) or mean + SEM (D and G). Statistical analysis: ***p < 0.001; **p < 0.01; *p < 0.05; ns, not significant by one-way ANOVA followed by Newman-Keuls post-test (B), by paired Student's t test (central versus peripheral for each condition, black), by one-way ANOVA followed by Tukey's post-test (peripheral among conditions, red; D), by two-way ANOVA followed by Tukey's post-test (E), and by one-way ANOVA followed by Tukey's post-test (G).

physiological growth brake that limits axon initiation and enables axon growth pauses. Axons have previously been observed to grow in spurts interrupted by pausing events [4, 58], which are less frequent in RhoA KO neurons. The periodic axon growth mediated by the RhoA-controlled growth brake could facilitate synchronization of axon elongation with the supply of building blocks necessary for growth. Moreover, as a premature arrival of axons would be disruptive for neuronal circuitry [59], slowing down axon growth may help the brain to mature in a coordinated fashion. In line with this concept, our data also indicate that RhoA could restrain the functional maturation of axons, delaying the onset of synaptic activity. We anticipate that decelerating axon growth and maturation might play a prominent role in the nervous system of mammals with long gestation periods, including humans, where axons grow relatively slowly [60].

Actin Arcs, the Physiological Brake to Axon Growth

Actin filaments and microtubules may generate two counteracting forces to keep axon growth in balance [11, 30, 61, 62]. Whereas actin filaments can create structures in the growth cone that halt axon elongation, protruding microtubules propel axon growth [48, 63–65]. What are the molecular mechanisms that allow conversion between axon growth and growth cone arrest? Using STED microscopy to investigate embryonic mouse

neurons, we detected actin arcs in the majority of WT growth cones, which previously have mainly been associated with the growth cones of stationary axons, such as those of *Aplysia* bag neurons [10]. This was in contrast to RhoA KO neurons, where only a few growth cones contained actin arcs, which initiated and extended axons quickly. Thus, actin arcs appear to be indicators of pausing axons.

The microtubule array in RhoA KO growth cones responded to the reorganization of their actin cytoskeleton. Microtubules in RhoA KO growth cones projected in bundles through a corridor-like structure flanked by actin filaments, an organization previously described for axons during the elongating phase [11]. Compared to microtubules in WT growth cones, microtubules in RhoA KO growth cones experienced less hindrance through the T-domain and, consequently, reached the growth cone's leading edge more frequently. The resulting faster growth of axons in RhoA KO neurons can be reversed by modest microtubule destabilization. Thus, RhoA regulates axon growth by controlling microtubule protrusion through the gating activity of actin arcs in the growth cone.

Myosin II, the Physiological Instructor of Actin Arcs Downstream of RhoA Restraining Axon Growth

Various signaling pathways and effector molecules downstream of RhoA were discussed as candidate regulators of neuronal polarity, including profilins, formins, ADF/cofilin, and myosins [2, 5, 17, 30, 66]. Our work demonstrates that genetic inactivation of RhoA leaves the G/F-actin ratio intact while leading to a partial inhibition of myosin II. This causes a decrease in actin arc formation along with microtubule protrusion to the axonal growth cone leading edge and accelerated axon growth without affecting axon specification. The partial inhibition of myosin II in RhoA KO neurons is likely due to its multiple sources of activation and deactivation, some of which are RhoA dependent, including ROCK and MYPT-1, whereas others are RhoA independent, including the myosin light chain kinase (MLCK) [67]. In fact, the RhoA KO phenotype is fully recapitulated by low doses of Blebb treatment. It argues that RhoA is less promiscuous during neuronal polarization than previously thought, revealing myosin II as the central physiologically relevant target.

Of note, the pool of inactivated myosin in neurons includes the highly expressed myosin IIB isoform and also myosin IIA, which is present at lower levels [19, 68, 69]. Myosin IIB and IIA differ in their kinetic properties, but they show overlapping functions [68] and undergo isoform-specific reorganizations in the axonal growth cone, depending on their growth substrates [35]. Given its expression levels in developing neurons, myosin IIB is likely to be a more relevant target effector for RhoA than myosin IIA. In this line, similar to RhoA ablation, deletion of myosin IIB or its replacement for a motor-impaired myosin IIB mutant during embryonic development leads to the destabilization of adherens junctions in the ventricular surface, resulting in the enlargement of the cerebral ventricles (hydrocephalus) [68, 69]. Future studies will decipher the specific contributions of these myosin isoforms to the regulation of neuron polarity.

In polarizing neurons, the actin network in the nascent axon is more susceptible to destabilization than that of future dendrites, an imbalance required to single out a fast-elongating axon [7]. Our data suggest that partial inhibition of myosin II or mild destabilization of the actin network, both contributing to relax the actomyosin system, leave the polarity program intact while facilitating its execution through early onset of axon formation and enhanced axon elongation. On the contrary, strong destabilization of the actomyosin system, by high doses of the myosin II inhibiting agent Blebb as well as actin-depolymerizing drugs, simply overrides the polarity program enabling multiple neurites to become axons [7–9, 23, 52]. It is interesting to consider the possibility that, besides its role as gatekeeper at the T-domain of axonal growth cones, the actomyosin system could also act globally as an intracellular corset that guides intrinsic neuronal polarization. Consistent with this view, the RhoA-dependent actomyosin cortical network is required to initiate membrane extensions during polarized growth in endothelial cells and in tumor-derived cell lines [70–72]. Thus, molecular manipulations that only relax but do not demolish the actin-myosin network would favor axon growth but still preserve polarity.

Conclusions

Multiple candidate molecules with promising instructive roles in early axon development have been identified. It has remained challenging, however, to unambiguously distinguish between molecules with essential roles in axon specification and those required only to regulate axon growth [73]. Here, we show that the physiological role of RhoA in neuronal polarization is to restrain the onset and the rate of axon growth, but not to specify the axon. RhoA functions by activating myosin II, which enables compaction of actin filaments to form actin arcs in the T-zone of the growth cone. These actin arcs restrain microtubule protrusion and, consequently, axon growth. Thus, this work defines a physiologically relevant molecular brake of axon growth during development.

It is noteworthy that the last two decades have seen enormous efforts to exploit the RhoA/ROCK pathway as a therapeutic tool to alleviate pathological and traumatic CNS conditions by inducing axon regeneration [74–76]. Given that axon regeneration is hypothesized to be a recapitulation of developmental processes [77] and that the cytoskeleton plays a key role during axon regeneration [64, 78, 79], this work has laid a promising basis to better understand the molecular mechanisms that could lead to axon regeneration.

STAR★METHODS

Detailed methods are provided in the online version of this paper and include the following:

- KEY RESOURCES TABLE
- LEAD CONTACT AND MATERIALS AVAILABILITY
- EXPERIMENTAL MODEL AND SUBJECT DETAILS
  - Animals
  - Transgenic Mice
- METHOD DETAILS
  - Neuronal Cell Culture
  - DNA Constructs and siRNAs
  - Cell Transfections
  - Antibodies and dyes
  - Immunocytochemistry
  - In Utero Electroporation (IUE)

SUPPLEMENTAL INFORMATION

Supplemental Information can be found online at https://doi.org/10.1016/j.cub.2019.09.040.

ACKNOWLEDGMENTS

We would like to thank Shweta Bendre, Artur Kania, Tien-Chen Lin, Kelly Kawabata-Galbraith, Thorben Pietralla, and Roland Wedlich-Söldner for critically reading and discussing the manuscript. We are grateful for the outstanding technical assistance of Jessica Gonyer, Liane Meyn, Blanca Randel, and Kerstin Weisheit. We would also like to thank staff members from the DZNE-Bonn animal facility for their dedicated assistance. We also extend our gratitude to Hans-Ulrich Fried, Kevin Keppler, and Ireen König from the DZNE light microscopy facility for their valuable support and to Manuel Schölling and Christoph Möhl from the DZNE image data analysis facility for their thoughtful statistical analysis of the data. We especially want to thank all the members of the F.B. laboratory for productive discussions related to this project. B.J.H. is supported by a Wings for Life (WfL) Aguayo-Tator Mentoring Fellowship and a non-stipendiary European Molecular Biology Organization (EMBO) long-term fellowship (ALTF 28-2017). This work was supported by IRP, WfL, DFG, ERANET AXON REPAIR, and ERANET RATER SCI (F.B.). F.B. is a member of the excellence cluster ImmunoSensation2, the SFBs 1089 and 1158, and is a recipient of the Roger de Spoelberch Prize.

AUTHOR CONTRIBUTIONS

S.D. and F.B. conceived the project; S.D. and F.B. designed research; S.D., B.J.H., A.H., T.E.S., C.H.C., and S.S. performed research; S.D. analyzed the data; C.B. provided mutant mice; F.B. supervised the research; and S.D. and F.B. wrote the paper. B.J.H., A.H., T.E.S., C.H.C., S.S., and C.B. provided feedback and contributed to editing the manuscript.

DECLARATION OF INTERESTS

The authors declare no competing interests.

Received: February 21, 2019
Revised: August 22, 2019
Accepted: September 16, 2019
Published: October 31, 2019

REFERENCES

1. Yogev, S., and Shen, K. (2017). Establishing neuronal polarity with environmental and intrinsic mechanisms. Neuron *96*, 638–650.
2. Takano, T., Xu, C., Funahashi, Y., Namba, T., and Kaibuchi, K. (2015). Neuronal polarization. Development *142*, 2088–2093.
3. Namba, T., Kibe, Y., Funahashi, Y., Nakamuta, S., Takano, T., Ueno, T., Shimada, A., Kozawa, S., Okamoto, M., Shimoda, Y., et al. (2014). Pioneering axons regulate neuronal polarization in the developing cerebral cortex. Neuron *81*, 814–829.
4. Dotti, C.G., Sullivan, C.A., and Banker, G.A. (1988). The establishment of polarity by hippocampal neurons in culture. J. Neurosci. *8*, 1454–1468.
5. Schelski, M., and Bradke, F. (2017). Neuronal polarization: from spatiotemporal signaling to cytoskeletal dynamics. Mol. Cell. Neurosci. *84*, 11–28.
6. Lewis, T.L., Jr., Courchet, J., and Polleux, F. (2013). Cell biology in neuroscience: cellular and molecular mechanisms underlying axon formation, growth, and branching. J. Cell Biol. *202*, 837–848.
7. Bradke, F., and Dotti, C.G. (1999). The role of local actin instability in axon formation. Science *283*, 1931–1934.
8. Bradke, F., and Dotti, C.G. (2000). Differentiated neurons retain the capacity to generate axons from dendrites. Curr. Biol. *10*, 1467–1470.
9. Kunda, P., Paglini, G., Quiroga, S., Kosik, K., and Caceres, A. (2001). Evidence for the involvement of Tiam1 in axon formation. J. Neurosci. *21*, 2361–2372.
10. Schaefer, A.W., Kabir, N., and Forscher, P. (2002). Filopodia and actin arcs guide the assembly and transport of two populations of microtubules with unique dynamic parameters in neuronal growth cones. J. Cell Biol. *158*, 139–152.
11. Lowery, L.A., and Van Vactor, D. (2009). The trip of the tip: understanding the growth cone machinery. Nat. Rev. Mol. Cell Biol. *10*, 332–343.
12. Ketschek, A.R., Jones, S.L., and Gallo, G. (2007). Axon extension in the fast and slow lanes: substratum-dependent engagement of myosin II functions. Dev. Neurobiol. *67*, 1305–1320.
13. Bradke, F., and Dotti, C.G. (2000). Establishment of neuronal polarity: lessons from cultured hippocampal neurons. Curr. Opin. Neurobiol. *10*, 574–581.
14. Bito, H., Furuyashiki, T., Ishihara, H., Shibasaki, Y., Ohashi, K., Mizuno, K., Maekawa, M., Ishizaki, T., and Narumiya, S. (2000). A critical role for a Rho-associated kinase, p160ROCK, in determining axon outgrowth in mammalian CNS neurons. Neuron *26*, 431–441.
15. Arimura, N., and Kaibuchi, K. (2007). Neuronal polarity: from extracellular signals to intracellular mechanisms. Nat. Rev. Neurosci. *8*, 194–205.
16. Namba, T., Funahashi, Y., Nakamuta, S., Xu, C., Takano, T., and Kaibuchi, K. (2015). Extracellular and intracellular signaling for neuronal polarity. Physiol. Rev. *95*, 995–1024.
17. Tahirovic, S., and Bradke, F. (2009). Neuronal polarity. Cold Spring Harb. Perspect. Biol. *1*, a001644.
18. Govek, E.E., Newey, S.E., and Van Aelst, L. (2005). The role of the Rho GTPases in neuronal development. Genes Dev. *19*, 1–49.
19. Kollins, K.M., Hu, J., Bridgman, P.C., Huang, Y.Q., and Gallo, G. (2009). Myosin-II negatively regulates minor process extension and the temporal development of neuronal polarity. Dev. Neurobiol. *69*, 279–298.
20. Cheng, P.L., Lu, H., Shelly, M., Gao, H., and Poo, M.M. (2011). Phosphorylation of E3 ligase Smurf1 switches its substrate preference in support of axon development. Neuron *69*, 231–243.
21. Conde, C., Arias, C., Robin, M., Li, A., Saito, M., Chuang, J.-Z., Nairn, A.C., Sung, C.-H., and Cáceres, A. (2010). Evidence for the involvement of Lfc and Tctex-1 in axon formation. J. Neurosci. *30*, 6793–6800.
22. Da Silva, J.S., Medina, M., Zuliani, C., Di Nardo, A., Witke, W., and Dotti, C.G. (2003). RhoA/ROCK regulation of neuritogenesis via profilin IIa-mediated control of actin stability. J. Cell Biol. *162*, 1267–1279.
23. Takano, T., Wu, M., Nakamuta, S., Naoki, H., Ishizawa, N., Namba, T., Watanabe, T., Xu, C., Hamaguchi, T., Yura, Y., et al. (2017). Discovery of long-range inhibitory signaling to ensure single axon formation. Nat. Commun. *8*, 33.
24. Pertz, O. (2010). Spatio-temporal Rho GTPase signaling - where are we now? J. Cell Sci. *123*, 1841–1850.
25. Lee, T., Winter, C., Marticke, S.S., Lee, A., and Luo, L. (2000). Essential roles of Drosophila RhoA in the regulation of neuroblast proliferation and dendritic but not axonal morphogenesis. Neuron *25*, 307–316.

26. Katayama, K., Leslie, J.R., Lang, R.A., Zheng, Y., and Yoshida, Y. (2012). Left-right locomotor circuitry depends on RhoA-driven organization of the neuroepithelium in the developing spinal cord. J. Neurosci. *32*, 10396–10407.

27. Leslie, J.R., Imai, F., Zhou, X., Lang, R.A., Zheng, Y., and Yoshida, Y. (2012). RhoA is dispensable for axon guidance of sensory neurons in the mouse dorsal root ganglia. Front. Mol. Neurosci. *5*, 67.

28. Cappello, S., Böhringer, C.R.J., Bergami, M., Conzelmann, K.-K., Ghanem, A., Tomassy, G.S., Arlotta, P., Mainardi, M., Allegra, M., Caleo, M., et al. (2012). A radial glia-specific role of RhoA in double cortex formation. Neuron *73*, 911–924.

29. Azzarelli, R., Kerloch, T., and Pacary, E. (2015). Regulation of cerebral cortex development by Rho GTPases: insights from in vivo studies. Front. Cell. Neurosci. *8*, 445.

30. Coles, C.H., and Bradke, F. (2015). Coordinating neuronal actin-microtubule dynamics. Curr. Biol. *25*, R677–R691.

31. Schaefer, A.W., Schoonderwoert, V.T.G., Ji, L., Mederios, N., Danuser, G., and Forscher, P. (2008). Coordination of actin filament and microtubule dynamics during neurite outgrowth. Dev. Cell *15*, 146–162.

32. Burnette, D.T., Ji, L., Schaefer, A.W., Medeiros, N.A., Danuser, G., and Forscher, P. (2008). Myosin II activity facilitates microtubule bundling in the neuronal growth cone neck. Dev. Cell *15*, 163–169.

33. Blanchoin, L., Boujemaa-Paterski, R., Sykes, C., and Plastino, J. (2014). Actin dynamics, architecture, and mechanics in cell motility. Physiol. Rev. *94*, 235–263.

34. Medeiros, N.A., Burnette, D.T., and Forscher, P. (2006). Myosin II functions in actin-bundle turnover in neuronal growth cones. Nat. Cell Biol. *8*, 215–226.

35. Turney, S.G., Ahmed, M., Chandrasekar, I., Wysolmerski, R.B., Goeckeler, Z.M., Rioux, R.M., Whitesides, G.M., and Bridgman, P.C. (2016). Nerve growth factor stimulates axon outgrowth through negative regulation of growth cone actomyosin restraint of microtubule advance. Mol. Biol. Cell *27*, 500–517.

36. Zhang, X.F., Schaefer, A.W., Burnette, D.T., Schoonderwoert, V.T., and Forscher, P. (2003). Rho-dependent contractile responses in the neuronal growth cone are independent of classical peripheral retrograde actin flow. Neuron *40*, 931–944.

37. Hilton, B.J., Blanquie, O., Tedeschi, A., and Bradke, F. (2019). High-resolution 3D imaging and analysis of axon regeneration in unsectioned spinal cord with or without tissue clearing. Nat. Protoc. *14*, 1235–1260.

38. Susaki, E.A., Tainaka, K., Perrin, D., Yukinaga, H., Kuno, A., and Ueda, H.R. (2015). Advanced CUBIC protocols for whole-brain and whole-body clearing and imaging. Nat. Protoc. *10*, 1709–1727.

39. Noctor, S.C., Martínez-Cerdeño, V., Ivic, L., and Kriegstein, A.R. (2004). Cortical neurons arise in symmetric and asymmetric division zones and migrate through specific phases. Nat. Neurosci. *7*, 136–144.

40. Wilde, C., Vogelsgesang, M., and Aktories, K. (2003). Rho-specific Bacillus cereus ADP-ribosyltransferase C3cer cloning and characterization. Biochemistry *42*, 9694–9702.

41. Garvalov, B.K., Flynn, K.C., Neukirchen, D., Meyn, L., Teusch, N., Wu, X., Brakebusch, C., Bamburg, J.R., and Bradke, F. (2007). Cdc42 regulates cofilin during the establishment of neuronal polarity. J. Neurosci. *27*, 13117–13129.

42. Tahirovic, S., Hellal, F., Neukirchen, D., Hindges, R., Garvalov, B.K., Flynn, K.C., Stradal, T.E., Chrostek-Grashoff, A., Brakebusch, C., and Bradke, F. (2010). Rac1 regulates neuronal polarization through the WAVE complex. J. Neurosci. *30*, 6930–6943.

43. Amano, M., Nakayama, M., and Kaibuchi, K. (2010). Rho-kinase/ROCK: a key regulator of the cytoskeleton and cell polarity. Cytoskeleton (Hoboken) *67*, 545–554.

44. Ohashi, K., Nagata, K., Maekawa, M., Ishizaki, T., Narumiya, S., and Mizuno, K. (2000). Rho-associated kinase ROCK activates LIM-kinase 1 by phosphorylation at threonine 508 within the activation loop. J. Biol. Chem. *275*, 3577–3582.

45. Maekawa, M., Ishizaki, T., Boku, S., Watanabe, N., Fujita, A., Iwamatsu, A., Obinata, T., Ohashi, K., Mizuno, K., and Narumiya, S. (1999). Signaling from Rho to the actin cytoskeleton through protein kinases ROCK and LIM-kinase. Science *285*, 895–898.

46. Arber, S., Barbayannis, F.A., Hanser, H., Schneider, C., Stanyon, C.A., Bernard, O., and Caroni, P. (1998). Regulation of actin dynamics through phosphorylation of cofilin by LIM-kinase. Nature *393*, 805–809.

47. Yang, N., Higuchi, O., Ohashi, K., Nagata, K., Wada, A., Kangawa, K., Nishida, E., and Mizuno, K. (1998). Cofilin phosphorylation by LIM-kinase 1 and its role in Rac-mediated actin reorganization. Nature *393*, 809–812.

48. Flynn, K.C., Hellal, F., Neukirchen, D., Jacob, S., Tahirovic, S., Dupraz, S., Stern, S., Garvalov, B.K., Gurniak, C., Shaw, A.E., et al. (2012). ADF/cofilin-mediated actin retrograde flow directs neurite formation in the developing brain. Neuron *76*, 1091–1107.

49. Tedeschi, A., Dupraz, S., Curcio, M., Laskowski, C.J., Schaffran, B., Flynn, K.C., Santos, T.E., Stern, S., Hilton, B.J., Larson, M.J.E., et al. (2019). ADF/cofilin-mediated actin turnover promotes axon regeneration in the adult CNS. Neuron *103*, 1073–1085.e6.

50. Amano, M., Ito, M., Kimura, K., Fukata, Y., Chihara, K., Nakano, T., Matsuura, Y., and Kaibuchi, K. (1996). Phosphorylation and activation of myosin by Rho-associated kinase (Rho-kinase). J. Biol. Chem. *271*, 20246–20249.

51. Kimura, K., Ito, M., Amano, M., Chihara, K., Fukata, Y., Nakafuku, M., Yamamori, B., Feng, J., Nakano, T., Okawa, K., et al. (1996). Regulation of myosin phosphatase by Rho and Rho-associated kinase (Rho-kinase). Science *273*, 245–248.

52. Flynn, K.C., Pak, C.W., Shaw, A.E., Bradke, F., and Bamburg, J.R. (2009). Growth cone-like waves transport actin and promote axonogenesis and neurite branching. Dev. Neurobiol. *69*, 761–779.

53. Riedl, J., Crevenna, A.H., Kessenbrock, K., Yu, J.H., Neukirchen, D., Bista, M., Bradke, F., Jenne, D., Holak, T.A., Werb, Z., et al. (2008). Lifeact: a versatile marker to visualize F-actin. Nat. Methods *5*, 605–607.

54. Stepanova, T., Slemmer, J., Hoogenraad, C.C., Lansbergen, G., Dortland, B., De Zeeuw, C.I., Grosveld, F., van Cappellen, G., Akhmanova, A., and Galjart, N. (2003). Visualization of microtubule growth in cultured neurons via the use of EB3-GFP (end-binding protein 3-green fluorescent protein). J. Neurosci. *23*, 2655–2664.

55. Schwamborn, J.C., and Püschel, A.W. (2004). The sequential activity of the GTPases Rap1B and Cdc42 determines neuronal polarity. Nat. Neurosci. *7*, 923–929.

56. Gonzalez-Billault, C., Muñoz-Llancao, P., Henriquez, D.R., Wojnacki, J., Conde, C., and Caceres, A. (2012). The role of small GTPases in neuronal morphogenesis and polarity. Cytoskeleton (Hoboken) *69*, 464–485.

57. Takano, T., Funahashi, Y., and Kaibuchi, K. (2019). Neuronal polarity: positive and negative feedback Signals. Front. Cell Dev. Biol. *7*, 69.

58. Bradke, F., and Dotti, C.G. (1997). Neuronal polarity: vectorial cytoplasmic flow precedes axon formation. Neuron *19*, 1175–1186.

59. Chédotal, A., and Richards, L.J. (2010). Wiring the brain: the biology of neuronal guidance. Cold Spring Harb. Perspect. Biol. *2*, a001917.

60. Pressler, R., and Auvin, S. (2013). Comparison of brain maturation among species: an example in translational research suggesting the possible use of bumetanide in newborn. Front. Neurol. *4*, 36.

61. Mitchison, T., and Kirschner, M. (1988). Cytoskeletal dynamics and nerve growth. Neuron *1*, 761–772.

62. Heidemann, S.R., and Buxbaum, R.E. (1994). Mechanical tension as a regulator of axonal development. Neurotoxicology *15*, 95–107.

63. Witte, H., Neukirchen, D., and Bradke, F. (2008). Microtubule stabilization specifies initial neuronal polarization. J. Cell Biol. *180*, 619–632.

64. Ruschel, J., Hellal, F., Flynn, K.C., Dupraz, S., Elliott, D.A., Tedeschi, A., Bates, M., Sliwinski, C., Brook, G., Dobrindt, K., et al. (2015). Axonal regeneration. Systemic administration of epothilone B promotes axon regeneration after spinal cord injury. Science *348*, 347–352.

65. Neukirchen, D., and Bradke, F. (2011). Cytoplasmic linker proteins regulate neuronal polarization through microtubule and growth cone dynamics. J. Neurosci. *31*, 1528–1538.
66. Kawabata Galbraith, K., and Kengaku, M. (2019). Multiple roles of the actin and microtubule-regulating formins in the developing brain. Neurosci. Res. *138*, 59–69.
67. Betapudi, V. (2014). Life without double-headed non-muscle myosin II motor proteins. Front Chem. *2*, 45.
68. Ma, X., Bao, J., and Adelstein, R.S. (2007). Loss of cell adhesion causes hydrocephalus in nonmuscle myosin II-B-ablated and mutated mice. Mol. Biol. Cell *18*, 2305–2312.
69. Tullio, A.N., Bridgman, P.C., Tresser, N.J., Chan, C.C., Conti, M.A., Adelstein, R.S., and Hara, Y. (2001). Structural abnormalities develop in the brain after ablation of the gene encoding nonmuscle myosin II-B heavy chain. J. Comp. Neurol. *433*, 62–74.
70. Fackler, O.T., and Grosse, R. (2008). Cell motility through plasma membrane blebbing. J. Cell Biol. *181*, 879–884.
71. Fischer, R.S., Gardel, M., Ma, X., Adelstein, R.S., and Waterman, C.M. (2009). Local cortical tension by myosin II guides 3D endothelial cell branching. Curr. Biol. *19*, 260–265.
72. Paluch, E., van der Gucht, J., and Sykes, C. (2006). Cracking up: symmetry breaking in cellular systems. J. Cell Biol. *175*, 687–692.
73. Polleux, F., and Snider, W. (2010). Initiating and growing an axon. Cold Spring Harb. Perspect. Biol. *2*, a001925.
74. Bond, L.M., Sellers, J.R., and McKerracher, L. (2015). Rho kinase as a target for cerebral vascular disorders. Future Med. Chem. *7*, 1039–1053.
75. McKerracher, L., and Guertin, P. (2013). Rho as a target to promote repair: translation to clinical studies with cethrin. Curr. Pharm. Des. *19*, 4400–4410.
76. Forgione, N., and Fehlings, M.G. (2014). Rho-ROCK inhibition in the treatment of spinal cord injury. World Neurosurg. *82*, e535–e539.
77. Hilton, B.J., and Bradke, F. (2017). Can injured adult CNS axons regenerate by recapitulating development? Development *144*, 3417–3429.
78. Hellal, F., Hurtado, A., Ruschel, J., Flynn, K.C., Laskowski, C.J., Umlauf, M., Kapitein, L.C., Strikis, D., Lemmon, V., Bixby, J., et al. (2011). Microtubule stabilization reduces scarring and causes axon regeneration after spinal cord injury. Science *331*, 928–931.
79. Blanquie, O., and Bradke, F. (2018). Cytoskeleton dynamics in axon regeneration. Curr. Opin. Neurobiol. *51*, 60–69.
80. Jackson, B., Peyrollier, K., Pedersen, E., Basse, A., Karlsson, R., Wang, Z., Lefever, T., Ochsenbein, A.M., Schmidt, G., Aktories, K., et al. (2011). RhoA is dispensable for skin development, but crucial for contraction and directed migration of keratinocytes. Mol. Biol. Cell *22*, 593–605.
81. Graus-Porta, D., Blaess, S., Senften, M., Littlewood-Evans, A., Damsky, C., Huang, Z., Orban, P., Klein, R., Schittny, J.C., and Müller, U. (2001). β1-class integrins regulate the development of laminae and folia in the cerebral and cerebellar cortex. Neuron *31*, 367–379.
82. Feng, G., Mellor, R.H., Bernstein, M., Keller-Peck, C., Nguyen, Q.T., Wallace, M., Nerbonne, J.M., Lichtman, J.W., and Sanes, J.R. (2000). Imaging neuronal subsets in transgenic mice expressing multiple spectral variants of GFP. Neuron *28*, 41–51.
83. Okabe, M., Ikawa, M., Kominami, K., Nakanishi, T., and Nishimune, Y. (1997). 'Green mice' as a source of ubiquitous green cells. FEBS Lett. *407*, 313–319.
84. Kaech, S., and Banker, G. (2006). Culturing hippocampal neurons. Nat. Protoc. *1*, 2406–2415.
85. Gomis-Rüth, S., Stiess, M., Wierenga, C.J., Meyn, L., and Bradke, F. (2014). Single-cell axotomy of cultured hippocampal neurons integrated in neuronal circuits. Nat. Protoc. *9*, 1028–1037.
86. Hermann, M., Stillhard, P., Wildner, H., Seruggia, D., Kapp, V., Sánchez-Iranzo, H., Mercader, N., Montoliu, L., Zeilhofer, H.U., and Pelczar, P. (2014). Binary recombinase systems for high-resolution conditional mutagenesis. Nucleic Acids Res. *42*, 3894–3907.
87. Weinberg, B.H., Pham, N.T.H., Caraballo, L.D., Lozanoski, T., Engel, A., Bhatia, S., and Wong, W.W. (2017). Large-scale design of robust genetic circuits with multiple inputs and outputs for mammalian cells. Nat. Biotechnol. *35*, 453–462.
88. Mizutani, K., Yoon, K., Dang, L., Tokunaga, A., and Gaiano, N. (2007). Differential Notch signalling distinguishes neural stem cells from intermediate progenitors. Nature *449*, 351–355.
89. Matsuda, T., and Cepko, C.L. (2004). Electroporation and RNA interference in the rodent retina in vivo and in vitro. Proc. Natl. Acad. Sci. USA *101*, 16–22.
90. Teruel, M.N., Blanpied, T.A., Shen, K., Augustine, G.J., and Meyer, T. (1999). A versatile microporation technique for the transfection of cultured CNS neurons. J. Neurosci. Methods *93*, 37–48.
91. Subauste, M.C., Von Herrath, M., Benard, V., Chamberlain, C.E., Chuang, T.H., Chu, K., Bokoch, G.M., and Hahn, K.M. (2000). Rho family proteins modulate rapid apoptosis induced by cytotoxic T lymphocytes and Fas. J. Biol. Chem. *275*, 9725–9733.
92. Beach, J.R., Licate, L.S., Crish, J.F., and Egelhoff, T.T. (2011). Analysis of the role of Ser1/Ser2/Thr9 phosphorylation on myosin II assembly and function in live cells. BMC Cell Biol. *12*, 52.
93. Benjamini, Y., and Hochberg, Y. (1995). Controlling the false discovery rate: a practical and powerful approach to multiple testing. J. R. Stat. Soc. B *57*, 289–300.

STAR★METHODS

KEY RESOURCES TABLE

REAGENT or RESOURCE	SOURCE	IDENTIFIER
Antibodies		
Mouse anti-Tubulin β 3 (TUBB3) Antibody	Biolegend	#801201; RRID: AB_2313773
Rabbit anti-β-Tubulin III antibody	Sigma	T2200; RRID: AB_262133
Mouse anti-GAPDH	Acris	ACR001P; RRID: AB_1616730
Mouse anti-Tau1 [PC1C6]	Millipore	MAB3420; RRID: AB_94855
Mouse anti-L1CAM [2C2]	Abcam	ab24345; RRID: AB_448025
Rabbit anti-Myosin Heavy Chain IIB	Cell Signaling	3404; RRID: AB_10829353
Mouse anti-LIMK	BD biosciences	611748; RRID: AB_399224
Rabbit anti-LIMK1/2 phospoThr508/505	Cell Signaling	3841; RRID: AB_2136946
Rabbit anti-RhoA	Cell Signaling	2117; RRID: AB_10693922
Rabbit anti-RhoB	Cell Signaling	2098; RRID: AB_2179103
Rabbit anti-RhoA (119)	Santa Cruz	sc-179; RRID: AB_632345
Mouse anti-Rac1 [23A8]	Millipore	05-389; RRID: AB_309712
Mouse anti-Cdc42	Cytoskeleton	ACD03; RRID: AB_10716593
Rabbit anti-Cofilin [D3F9]	Cell Signaling	5175; RRID: AB_10622000
Rabbit anti-Cofilin phospho (Ser3) [77G2]	Cell Signaling	3313; RRID: AB_2080597
Mouse-anti Cofilin	Abcam	ab54532; RRID: AB_941092
Rabbit anti-Myosin light chain 2 (MLC2)	Thermo Fisher	PA5-17624; RRID: AB_10985405
Mouse anti-MLC2 (phospho-Ser19)	Thermo Fisher	MA5-15163; RRID: AB_10979087
Rabbit anti-MLC2 (phosphor-Ser20)	Abcam	ab2480; RRID: AB_303094
Mouse anti-MYPT-1	BD biosciences	612164; RRID: AB_399535
Rabbit anti-MYPT-1 (phospho-Thr696)	Cell Signaling	5163; RRID: AB_10691830
Mouse anti-SatB2	Abcam	ab51502; RRID: AB_882455
Rabbit anti-Tbr1	Abcam	ab31940; RRID: AB_2200219
Rat anti-Ctip2 [25B6]	Abcam	ab18465; RRID: AB_10015215
Rabbit anti-pan actin	Cytoskeleton	AAN01; RRID: AB_10708070
Goat anti-mouse Alexa Fluor 488	Thermo Fisher	A-11029; RRID: AB_138404
Goat anti-rabbit Alexa Fluor 488	Thermo Fisher	A-11034; RRID: AB_2576217
Goat anti-rabbit Alexa Fluor 350	Thermo Fisher	A-10039; RRID: AB_2534015
Goat anti-rat Alexa Fluor 647	Thermo Fisher	A-21247; RRID: AB_141778
Goat anti-rabbit Alexa Fluor 594	Thermo Fisher	A-11037; RRID: AB_2534095
Goat anti-mouse Alexa Fluor 568	Thermo Fisher	A-11031; RRID: AB_144696
Phalloidin-Rhodamine	Thermo Fisher	R415; RRID: AB_2572408
Phalloidin-Atto647N	Sigma	65906
Mouse-IgG-Atto 647N	Sigma	50185; RRID: AB_1137661
4′,6-diamidino-2-phenylindole (DAPI)	Thermo Fisher	D1306; RRID: AB_2629482
Sheep-Anti-mouse IgG-HRP	GE Healthcare	NA931; RRID: AB_772210
Donkey-Anti-rabbit IgG-HRP	GE Healthcare	NA934; RRID: AB_772206
Chemicals, Peptides, and Recombinant Proteins		
Rho Inhibitor 1 (C3T)	Cytoskeleton	CT04
Nocodazol	Sigma	M1404
(-)-Blebbistatin	Sigma	B0560
Horse serum	Pan-Biotech	P30-0702
Fetal calf serum	Thermo Fisher	16140063
Normal goat serum	Sigma	G9023

(*Continued on next page*)

Continued

REAGENT or RESOURCE	SOURCE	IDENTIFIER
Poly-L-lysine	Sigma-Aldrich	P2636
Neuropan-2 supplement	Pan-Biotech	P07-11010
B27 supplement	Thermo Fisher	17504044
Bradford Solution	Applichem	A6932,0250
Ripa Lysis Buffer 10X	Merck	20-188
Low melting point GP Agarose	Byozim	850111
Critical Commercial Assays		
Elisa-based 96-well ROCK assay kit	Cell Biolabs	STA-416
RhoA / Rac1 / Cdc42 Activation Assay Combo Biochem Kit (bead pull-down format)	Cytoskeleton	BK030
G/F actin kit	Cytoskeleton	BK037
Mouse Neuron Nucleofector Kit	Amaxa	VPG-1001
QIAGEN Plasmid Plus Maxi Kit	QIAGEN	12963
PhosSTOP	Roche	04906845001
Complete, Mini, EDTA-free Protease Inhibitor Cocktail	Roche	11836170001
Pierce ECL Western Blotting Substrate	Thermo Fisher	32106
SuperSignal West Dura Extended Duration Substrate	Thermo Fisher	34075
Experimental Models: Organisms/Strains		
RhoA floxed mice	Professor Cord Brakebusch [80]	N/A
Nestin-Cre mice [B6.Cg-Tg(Nes-cre)1Kln/J]	The Jackson laboratory [81]	003771; RRID: IMSR_JAX:003771
Thy1-GFP-M mice [STOCK Tg(Thy1-EGFP)MJrs/J]	The Jackson laboratory [82]	007788; RRID: IMSR_JAX:007788
CAG-GFP mice [C57BL/6-Tg(CAG-EGFP)1Osb/J]	The Jackson laboratory [83]	003291; RRID: IMSR_JAX:003291
C57BL/6J	Charles Rivers	JAX C57BL/6J; RRID: IMSR_JAX:000664
Oligonucleotides		
See Table S1	N/A	N/A
Recombinant DNA		
See Table S2	N/A	N/A
Software and Algorithms		
ImageJ	NIH	RRID: SCR_002074; https://imagej.nih.gov/ij/
AxioVision microscope software	Zeiss	RRID: SCR_002677; N/A
ZEN Digital Imaging for Light Microscopy (Zen Blue) software	Zeiss	RRID: SCR_013672
SoftWoRx 3.5.0 imaging software	Applied Precision	N/A
Leica Application Suite X (LAX) 3.1.5.1638	Leica	N/A
Imaris 9.2	Bitplane	N/A
Huygens professional deconvolution software, version 17.04	Scientific Volume Imaging, the Netherlands, http://svi.nl	RRID: SCR_014237
Custom-made Fisher's Permutation Test corrected for multiple comparison error by Benjamini-Hochberg procedure; confidence level $\alpha = 0.05$ for quantification of neuron distribution in brain areas.	Dr. Christoph Moehl, Image and Data Analysis Facility, DZNE Bonn	https://pypi.python.org/pypi/permutation_test/0.18
Ordinal logistic regression model for the analysis of morphological stages during development	Dr. Manuel Scholling, Image and Data Analysis Facility, DZNE Bonn	https://cran.rproject.org/web/packages/MASS/
Generalized linear model (GLM) for the analysis of axon length during development using a Gamma distribution to account for the non-negative range of the length plus correction for confounding effects of the individual experiments	Dr. Manuel Scholling, Image and Data Analysis Facility, DZNE Bonn	https://www.Rproject.org/
Axon growth kinetics script for Phyton	Dr. Manuel Scholling, Image and Data Analysis Facility, DZNE Bonn	https://nextcloud.dzne.de/index.php/s/AeOZTNgco8rxp1j/Download

(*Continued on next page*)

Continued

REAGENT or RESOURCE	SOURCE	IDENTIFIER
Customized ANOVA test (F-test) (Figure 1B; see Key Resources Table)	Dr. Manuel Scholling, Image and Data Analysis Facility, DZNE Bonn	http://www.scipy.org/
AXON pclamp 11 (electrophysiology data acquisition)	Molecular Devices	https://www.moleculardevices.com/
AXON clampfit 11 (electrophysiology data analysis)	Molecular Devices	https://www.moleculardevices.com/
Prism 8	GraphPad Software	Version 8.0.0
Other		
TCS SP8 STED 3X plus 775-nm pulsed laser	Leica	N/A
DeltaVision RT	Applied Precision	N/A
Microscope Axio Observer D1	ZEISS	590636
Confocal microscope LSM700	ZEISS	N/A
2-photon microscope LSM 7MP	ZEISS	N/A
Cryostat CM3050S	Leica	N/A
Vibratome VT1200S	Leica	N/A
Immobilon-PSQ PVDF Membrane	Merck Millipore	ISEQ00010
Nucleofector Device	Lonza	AAB-1001
Embedding cryo-gel (Surgipath)	Leica	REF 39475237
Decloaking ChamberTM NxGEN	Biocare	DC2012-220V
35 mm Dish, No. 1.5 Coverslip, 14 mm Glass Diameter, Uncoated	MatTek	P35G-1.5-14-C
35 mm Dish, No. 1.5 Coverslip, 20 mm Glass Diameter, Uncoated	MatTek	P35G-1.5-20-C
13 mm glass coverslips	Marienfeld	#01-115 30
35 mm CELLVIEW 4-well Glass bottom culture dish	Greiner bio-one	62775
50 mm (35 mm transwell) plates (Fluorodish)	World Precision Instruments (WPI)	FD5040-100
30 mm Polytetrafluoroethylene (*PTFE*) membranes	Millipore	PICM03050
ProLong Gold Antifade Mountant	Thermo Fisher	P36930
Acetylated BSA (BSA-c)	Aurion	900-099
Fluoromount Aqueous mounting medium	Sigma	F4690
ForaneR Isoflurane	Abbot	B506
LN Scope for electrophysiology (upright microscope incl. motorized focus and micromanipulators, CCD camera)	Luigs&Neumann	N/A
AXON Multiclamp 700B; electrophysiology amplifier	Molecular Devices	AXOMULT700
DIGIDATA 1550B; electrophys data acquisition system	Molecular Devices	DIGIDATA1550

LEAD CONTACT AND MATERIALS AVAILABILITY

The plasmids generated in this study have been deposited to Addgene (see Table S2). Further information and requests for resources and reagents should be directed to and will be fulfilled by the Lead Contact, Frank Bradke (frank.bradke@dzne.de). There are no restrictions on any data or materials presented in this paper.

EXPERIMENTAL MODEL AND SUBJECT DETAILS

Animals

All animal experiments were performed in accordance with the Animal Welfare Act and the guidelines of the North Rhine-Westphalia State Environment Agency (Landesamt für Natur, Umwelt und Verbraucherschutz (LANUV)). The animals were group housed (up to 5 mice per cage) with room temperature controlled at 21–22°C, and an artificial 12-h light:dark cycle (lights off at 6:00 pm). Mice were given food and water *ad libitum* throughout the experiment.

Transgenic Mice

CNS conditional RhoA KO mice

To obtain RhoA ablation in the nervous system we used a mouse line, with exon 3 of the *RhoA* gene flanked by loxP sites, referred to as $RhoA^{fl/fl}$ [80]. To obtain mouse embryos with a CNS conditional ablation of RhoA, $RhoA^{fl/fl}$ mice were first mated with a transgenic

Nestin-Cre driver line [81] to generate *nes-cre*$^{tg/-}$, *RhoA*$^{fl/wt}$ mice that were subsequently crossed with homozygous *RhoA*$^{fl/fl}$ mice. The mating yielded embryos with genotypes in the expected Mendelian ratios including nes-cre$^{tg/-}$, *RhoA*$^{fl/fl}$, here on referred as RhoA KO, and nes-cre$^{-/-}$, *RhoA*$^{fl/fl}$ control littermates here on referred as WT. To obtain sparse GFP neuronal labeling in adult RhoA KO mice, we first generate *RhoA*$^{fl/fl}$,*gfp-m*$^{tg/tg}$ mice by mating *RhoA*$^{fl/fl}$ and *gfp-m*$^{tg/tg}$ [82] to obtain a *RhoA*$^{fl/wt}$,*gfp-m*$^{tg/-}$ F1. F1 mice were then inter-crossed until obtaining progeny that showed homozygosity for both transgenes. These mice were then crossed with *nes-cre*$^{tg/-}$,*RhoA*$^{fl/wt}$ mice to obtain RhoA KO[GFP] (nes-cre$^{tg/-}$,*RhoA*$^{fl/fl}$;*gfp-m*$^{tg/-}$) and WT[GFP] (*nes-cre*$^{-/-}$,*RhoA*$^{fl/fl}$;*gfp-m*$^{tg/-}$) mice. Mice ubiquitously expressing enhanced green fluorescent protein (EGFP)-mice under a "CAG" promoter [83] were from the Jackson laboratory. All mice were kept on a C57BL/6J background.

METHOD DETAILS

Neuronal Cell Culture

Cell Culture

Primary hippocampal neurons were obtained from embryonic day 16.5 (E16.5) to E17.5 mouse embryos. Glia-free cultures were performed similarly to as previously described [84]. In brief, after dissection, hippocampi were collected in HBSS (Thermo Fisher). For RhoA KO cultures, we followed the same procedure but processing the hippocampi from individual embryos separately to maintain genetic identity of the subsequent cultures. Next, hippocampi were digested in trypsin 0.05% (Thermo Fisher) for 15 min and the reaction was stopped by addition of MEM-horse serum (MEM-HS) media [1X MEM, 1X essential and non-essential amino acids, 2mM L-glutamine (all from Thermo Fisher), 0.22% $NaHCO_3$, 0.6% glucose and 10% horse serum (Pan-Biotech)]. Hippocampi were then mechanically dissociated with fire-polished glass-Pasteur pipettes.

Dissociated neurons were plated either at low (71 cells/mm^2) or high (350 cells/mm^2) density for visualization experiments or biochemistry, respectively. For all culture conditions, neurons were allowed to attach to Poly-L-lysine-coated coverslips in the presence of MEM-HS for 2 h, which was then replaced for neuronal media (N2) (1X MEM, sodium pyruvate 1 mM, Neuropan 2 supplement 1% (Pan-Biotech), $NaHCO_3$, 0.6% glucose, 2 mM L-glutamine) pre-conditioned by 2-3 days incubation with a feeder layer composed of WT glia. While glia-conditioned N2 was used in short-term cultures (12-48 h), long-term cultures (> DIV 4) required continuous support of a glial feeder layer [84].

Drugs treatments were carried out during the change to neuronal glia-conditioned N2 media [Blebbistatin 0.5 μM and 20 μM (Sigma), Latrunculin A 5 nM and 25 nM (Biomol), Nocodazole 50 nM (Sigma) and C3T 0.5 μg/ml (Cytoskeleton)]. Glia-conditioned N2 containing the C3T was replaced for fresh glia-conditioned N2 4 h after addition following manufacturer's recommendations. To note, extra care has to be taken to dilute nocodazole to avoid precipitation, which can cause toxicity and high variability in the drug's effective concentration.

Mixed WT [green fluorescent protein (GFP)-positive]/RhoA KO (GFP-negative) cultures were performed similarly to as previously described [85]. In short, embryonic hippocampal neurons isolated from RhoA KO embryos were cultured alongside with WT neurons ubiquitously expressing EGFP obtained from age-matched EGFP-mice embryos [41, 83, 85].

Unless otherwise indicated, the immunocytochemistry experiments are performed with cultured hippocampal neurons and the neuronal extracts for immunoblot analysis were prepared from cultured cortical neurons.

DNA Constructs and siRNAs

Recombination reporters pCAG-loxSTOPlox-ZsGreen and pCAG-roxSTOProx-ZsGreen as well as pCAG-NLS-HA-Dre were a gift from Pawel Pelczar (Addgene plasmids # 51269, 51274 and 51272 respectively [86]. To prepare pTα1-iCre and pTα1-Dre, iCre and Dre sequences were amplified from pCAG-iCre [a gift from Wilson Wong (Addgene plasmid # 89573 [87]] and pCAG-NLS-HA-Dre with the following primers: iCre-forward, iCre-reverse, Dre-forward and Dre-reverse (see Table S1). The amplified sequences were later combined by overlapping PCR with the sequence coding for the Tubulin-alpha-1 promoter (Tα1) amplified from T alpha 1p-DsRed2 (pTα1-DsRed2) [a gift from Nicholas Gaiano (Addgene plasmid # 17707 [88];] with the primers: Tα1-forward and Tα1-reverse (see Table S1). The assembled products were sub-cloned in a pCAGIG backbone [a gift from Connie Cepko (Addgene plasmid # 11159 [89];] in SpeI/BglII sites. The Cre/Lox recombination reporter pCAG-loxSTOPlox-LynEGFP was generated as follows: A DNA coding EGFP fused to the membrane targeting motif of Lyn kinase (LynEGFP) was amplified from PM-GFP [a gift from Tobias Meyer (Addgene plasmid # 21213 [90]] with the primers lox-LynEGFP-forward and lox-LynEGFP-reverse (see Table S1), and cloned into a pCAG-loxSTOPlox-ZsGreen backbone where ZsGreen was removed between PstI/SacI sites. To generate the "mock" Dre/Rox recombination reporter pCAG-roxSTOProx-LynEGFP, a roxSTOProx cassette was amplified from pCAG-roxSTOProx-ZsGreen with the primers roxSTOP-Lyn-forward and roxSTOP-Lyn-reverse (see Table S1) and inserted into pCAG-loxSTOPlox-LynEGFP into SalI/PstI sites replacing the loxSTOPlox cassette. To generate the pCMVd1-EGFP-hRhoA-wt plasmid, where EGFP-hRhoA is expressed under a minimal CMV promoter, EGFP-hRhoA-wt was excised from pcDNA3-EGFP-RhoA-wt [a gift from Gary Bokoch (Addgene plasmid # 12965 [91];) with HindIII/XhoI and inserted within the same sites in a FN22K HaloTag*CMVd1Flexi®Vector (Promega). For the overexpression of MLC2 CA in cultures, a bicistronic vector was prepared as follows. MLC2 CA was amplified from pEGFP-MRLC1 T18D, S19D [a gift from Tom Egelhoff (Addgene plasmids # 35681 [92];) with the primers MLC(XhoI)-forward and MLC(SalI)-reverse (see Table S1). PCR product was digested with XhoI/SalI and cloned into a XhoI site in a pCAGIG vector resulting in a bicistronic pCAG-MLC2(CA)-IRES-GFP.

For the combined expression of LifeAct-GFP and EB3-mCherry under independent promoters, a dual CMV promoter vector (pCMV-EB3mCherry_cmv-LifeActGFP) was generated as follow: A CMV-LifeAct-GFP-polyA cassette was amplified from Lifeact-GFP [53] with primers SpeI-CMV-forward 5′- and BglII-EGFP-reverse (see Table S1), and inserted in SpeI/BglII sites of pCAGIG (pCMV-lifeAct-GFP). Then, a CMV-EB3-mCherry-polyA cassette was amplified from a EB3-mCherry plasmid [54] with primers SalI-CMV-forward and SpeI-sv40-reverse (see Table S1), and cloned in SalI/SpeI sites of pCMV-lifeAct-GFP prepared before. Finally, to generate a pTub-alpha1-EGFP, a pTub-alpha-1-DsRED vector was digested with NdeI/BamHI to release the Ta1 sequence that was subsequently cloned into a pCMV-EGFP-N1 vector (Clontech) where the CMV promoter was removed by digestion with AseI/BglII. All these complementary restriction sites were destroyed. All primers were from Sigma. PCRs were performed with Phusion High-Fidelity PCR Master Mix (New England Biolabs). Vector Cloning was performed following the Gibson assembly method using the NEBuilder HiFi DNA Assembly Cloning Kit (New England Biolabs), or regular T4 ligase-based cloning (Thermo Fischer).

For gene silencing experiments, siRNA oligos (Silencer® Select) and RNAi negative control were purchased from Thermo Fisher (see Table S2).

Cell Transfections

Cell transfections were performed using a Nucleofector Device (program 0-005, Lonza) and the mouse neuron Nucleofector® Kit (Amaxa) according to the manufacturer's specifications. 5×10^5 cells were used for each transfection with 3 μg of plasmid DNA. All DNAs were prepared with EndoFree Maxiprep kit (QIAGEN). For the silencing experiments, 5×10^5 cells were transfected with a mix of 0.2 pmol of the siRNA and 1 μg of neuron-specific GFP expressing plasmids (pTub-alpha1-EGFP) as carrier DNA and transfection reporter.

Antibodies and dyes

Antibodies

The following primary antibodies were used: Mouse anti-βIII tubulin (Tuj1, Covance), rabbit anti-βIII tubulin (Sigma), mouse anti-Glyceraldehyde 3-phosphate Dehydrogenase (GAPDH, Acris), mouse anti-Tau1 [PC1C6] (Millipore), rabbit anti-Myosin Heavy Chain IIB (Cell Signaling), mouse anti-LIMK (BD biosciences), rabbit anti-LIMK1/2 phospoThr508/505 (Cell Signaling), rabbit anti-RhoA (Cell Signaling), rabbit anti-RhoB (Cell Signaling), rabbit anti-RhoA (119) (Santa Cruz), mouse anti-Rac1 [23A8] (Millipore), mouse anti-Cdc42 (Cytoskeleton), rabbit anti-Cofilin [D3F9] (Cell Signaling), rabbit anti-Cofilin phospho (Ser3) [77G2] (Cell Signaling), mouse-anti Cofilin (Abcam), rabbit anti-Myosin light chain 2 (MLC2) (Thermo Fisher), mouse anti-MLC2 (phospho-Ser19) (Thermo Fisher), rabbit anti-MLC2 (phosphor-Ser20) (Abcam), mouse anti-MYPT-1 (BD biosciences), rabbit anti-MYPT-1 (phospho-Thr696) (Cell Signaling), mouse anti-SatB2 (Abcam), rabbit anti-Tbr1 (Abcam), rat anti-Ctip2 [25B6] (Abcam). The following secondary antibodies and dyes were used: Alexa Fluor (488, 350, 647, 594 and 568), Phalloidin-Rhodamine and 4',6-diamidino-2-phenylindole (DAPI) were from, Thermo Fisher.; anti-mouse IgG-horse radish peroxidase (HRP) and anti-rabbit IgG-HRP were from (GE Healthcare); Phalloidin-Atto647N and mouse-IgG-Atto 647N were from Sigma.

Immunocytochemistry

Neuronal cultures were fixed with 4% paraformaldehyde, 4% sucrose for 20 min except for cultures used for STED microscopy, where fixation was performed under conditions optimal for the preservation of the cytoskeleton: 4% paraformaldehyde, 4% sucrose in PHEM fixation buffer (300 mM PIPES, 125 mM HEPES, 50 mM EGTA, 10 mM $MgCl_2$, pH = 6.9 [63]; for 15 min. Fixed cells were quenched with 50 mM NH_4CL or 0.1 M Glycine (for fixation with PFA or PHEM respectively) for 15 min and extracted with 0.1% Triton X-100 in PBS for 5 min. The coverslips with the cells were washed three times with PBS then blocked at room temperature (RT) for 1 h. Depending on the antibodies used, blocking agents were 3% Bovine Serum Albumin (BSA, Sigma; for the antibodies bold-highlighted in the list above), blocking buffer (2% Fetal Bovine Serum (FBS, Thermo Fisher), 2% BSA and 0.2% fish gelatin (Sigma) in PBS) or (Acetylated BSA (BSA-c, Aurion) for STED experiments. After blocking, cells were incubated with the primary antibodies at RT for 3 h or overnight at 4°C. Cells were washed three times with PBS and incubated with the secondary antibodies (1:800) at RT for 1 h. The antibodies and dyes were mixed in a 1:10 dilution of the agent used in the blocking step. Cells were washed, rinsed and mounted onto microscope slides with Fluouromount™ (Sigma) or, for STED experiments, with ProLong™ Diamond (Thermo Fisher). Images were taken in a random fashion using an Axiovert observer D1 microscope equipped with a high performance CCD camera (Axiocam MRn) and Zen Blue software (all from Zeiss) with the following objectives: LCI Plan-Neofluar 25X/0.8 oil, Plan-Apochromat 40X/1.3 oil, Plan-Apochromat 63X/1.4 oil, and A Plan-Apochromat 100X/1.4 oil.

STED Microscopy

STED images were acquired with a TCS SP8 STED 3X equipped with a 775 nm depletion lasers and a HCX PL APO 100X/1.4 oil Objective (Leica) using the Leica Application suite X (LAX) 3.1.5.1638 software platform. Probes labeled with AlexaFluor 647 and Atto647N were excited with the 647 nm wavelength of a white light laser (WLL) and depleted with a continuous wave (CW) 775 nm STED laser. Probes labeled with AlexaFluor 594 were excited with the 594 wavelength of a WLL laser and depleted with a CW 775 nm STED laser. Hybrid detectors (HyD, Leica) were used with a gating time (tg) of $0.3 \leq tg \leq 6$ ns. Pixel size was chosen at 20 nm. STED images were deconvolved using Huygens Professional Deconvolution software (Scientific Volume Imaging, Netherlands). Images were analyzed using ImageJ software (NIH).

In Utero Electroporation (IUE)

Timed-pregnant mice carrying *RhoA*$^{fl/fl}$ embryos were anesthetized under a constant flow of Isoflurane (Abbot) and the uterus was carefully exposed from the abdominal cavity. Throughout the surgery, warm saline was used to prevent dehydration. The lateral ventricles of the embryos (E12.5 or E13.5 depending on the experiment) were filled with 2-3 μl of a 10:1 mix of EndoFree DNA and Fast Green dye using micropipettes pulled in a pipette-puller devise (Zeitz) and a Picospritzer III microinjection device (Intracel). The DNAs used for electroporation include pTa1-iCre, pCAG-loxSTOPlox-ZsGreen, pCAG-roxSTOProx-ZsGreen, pTa1-Dre, pCAG-loxSTOPlox-LynEGFP and pCAG-roxSTOProx-LynEGFP. Forceps-type electrode paddles (Platinum Tweezertrode) controlled by an ECM 830 electroporator (both from BTX Harvard Apparatus) were used to deliver 5 pulses at 35 mV with 50 ms durations and 600 ms intervals. Following the electroporation of all embryos, the uterus was returned into the abdomen, which was carefully stitched. Depending on the experiment, the mother was sacrificed at either E14.5 or E15.5. The brains were extracted from the embryos and processed for histological analysis.

Ex Utero Electroporation (EUE) and Organotypic Culture of Brain Slices

E13.5 *RhoA*$^{fl/fl}$ embryos were extracted from the uterine sack, injected with either pair of plasmids pTa1-iCre / pCAG-loxSTOPlox-LynEGFP or pTa1-Dre / pCAG-roxSTOProx-LynEGFP, and electroporated. The same electrodes and electroporator described for the IUE procedure above were used to deliver 5 pulses at 54 mV with 50 ms durations and 1 s intervals. Immediately after, the heads of the embryos were collected in Gey's Balanced Salt Solution (GBSS, Sigma) supplemented with 0.5% glucose (GBSS-Glucose) and the brains extracted under scope. The brains were subsequently embedded in 3% low-melting point agarose (Biozym) and cut in 300 μm thick coronal sections (flanking the electroporated areas) using a VT1200 vibratome (Leica). Brains were always kept and cut in cold GBSS-Glucose. The brain slices were placed on 30 mm Polytetrafluoroethylene (PTFE) membranes (Millipore) in 35 mm transwell plates (Fluorodish, WPI) with slice media [Neurobasal 1X, FCS 5%, B27 supplement 1:50, Glutamax 1:400, penicillin/streptomycin 1:200 (all from Thermo Fisher), horse serum 5%, Neuropan-2 supplement 1:100 (from Pan-Biotech) pH = 7.3]. 20 h after culturing them, sections were imaged for additional 48 h with a DeltaVision RT (Applied Precision) live-cell imaging setup based on an Olympus IX71 inverted microscope, with a CO_2 regulated incubation chamber maintained at 35°C (Solent Scientific) and an objective UPlanSApo 10x/0.40 infinity/0.17/FN26.5 (Olympus). Images were acquired with a Photometrics CoolSnap HQ camera (Roper Scientific) using SoftWoRx 3.5.0 imaging software (Applied Precision). 20 μm z stack scans of multiple tiles around the areas of interest were taken every 20 min. Stitching of the tiles was performed in ImageJ (NIH) with a custom-made script (see Key Resources Table).

Immunohistochemistry

The heads of the mouse embryos were fixed in 4% paraformaldehyde, 4% sucrose in phosphate-buffered saline (PBS) at RT for 2 h and then at 4°C overnight. The fixed heads were incubated in 30% sucrose in PBS for 48 h. Brain were extracted, rinsed in PBS, embedded in Surgipath® cryo-gel (Leica) and frozen. The frozen brains were then cut with a cryostate (Leica) into 25-50 μm thick coronal sections and adhered to positive charged microscopy slides (Superfrost, Thomas Scientific). The brain sections were warmed at 37°C and the cryoembedding medium washed with PBS. For nuclear staining of transcription factors, antigen retrieval was performed by incubating the brain sections in citrate buffer (Citrate 10 mM, Glycerol 10% plus Tween 0.05% pH = 6) at 90°C for 30 min in decloaking chamber (Biocare). Then, cryosections were quenched with Glycine 0.1M for 30 min, permeabilized in 0.3% Triton X-100 for 1 h and blocked with normal goat serum (NGS, Sigma) 5% plus 0.2% Triton X-100 in PBS (all performed at RT) for 1 h. For the nuclear staining of transcription factors, the blocking step was avoided. Section were then incubated overnight at 4°C with the primary antibodies previously diluted in 1% NGS containing 0.2% Triton X-100 in PBS. After washing three times with PBS, cryosections were incubated with Alexa Fluor conjugated secondary antibodies (1:200) at RT for 3 h. When indicated, sections were incubated with DAPI (1:20000) for 10 min. Confocal stacks were acquired with a Plan-Apochromat 20X/0.8 air objective using a LSM700 confocal microscope (Zeiss). The maximum intensity projection images used for display were produced using Zen software (Zeiss). Images were analyzed using ImageJ software (NIH).

G/F-actin assay

Filamentous (F) and Globular monomeric (G) actin were fractionated from WT and RhoA KO neuronal cultures using a centrifugation-based G-actin/F-actin *in-vivo* assay kit (Cytoskeleton). Cultured neurons were lysed and processed according to the manufacturer's guidelines. The resulting fractions were analyzed by Immunoblot using an anti-pan actin antibody provided by the kit (Cytoskeleton).

Pull-down assays

For the determination of the active status of GTPases, we used a beads pull-down-based RhoA / Rac1 / Cdc42 Activation Assay Combo Kit (Cytoskeleton) WT and RhoA KO neurons cultured for 20 h were lysed and processed according to the manufacturer's guidelines. Approximately 150-200 μg of total protein were used for each pull-down experiment. Individual culture samples were processed separately on ice to allow complete preparation within 5 min from the removal of the culture media. The resulting fractions were determined by Immunoblot.

Immunoblotting

Cultured cells were lysed on ice in RIPA buffer (Millipore) containing phosphatase (PhosSTOP, Roche) and protease inhibitors (Complete, Roche). Lysates were centrifuged and the supernatant collected. Protein concentration in the lysate was determined using the Bradford Reagent (Applichem). Lysates were mixed 4:1 with 5X homemade Laemmli buffer (25% 2-Mercaptoethanol, 0.05% Bromophenol blue, 50% Glycerol, 10% SDS (electrophoresis-grade), 0.31M Tris-HCl (pH 6.8)), boiled at 95°C and fractioned by 3-(N-morpholino)propanesulfonic acid (MOPS)/SDS-polyacrylamide gel electrophoresis (PAGE). The separated proteins were transferred to polyvinylidene difluoride (PVDF, Millipore) membrane and stained with Ponceau S (Applichem) to verify the transfer of the samples and confirm equal loading. Membranes were blocked at RT with 5% skimmed-milk or 5% bovine serum albumin (for antibodies bold-highlighted in the list above) in Tris-Buffered Saline (TBS) plus 0.1% Tween20 (TBS-T) for 1 h. Primary antibodies were diluted in TBS-T and incubated with the membrane for 3 h at RT or overnight at 4°C. The secondary antibodies were sheep anti-mouse or goat anti-rabbit IgG-HRP (GE Healthcare), and the blots were developed using either Pierce ECL Western Blotting Substrate or SuperSignal West Dura (both from Thermo Fischer).

ROCK Activity Assay

To determine ROCK activity we used an ELISA-based 96-well ROCK assay kit (Cell Biolabs). WT and RhoA KO neurons cultured for 20 h were lysed and processed according to the manufacturer's guidelines. Briefly, 5 μg of total protein was incubated 30 min at 30°C in presence of the ROCK substrate. The reaction mixture was washed and the in-well substrate immunolabeled following the provider's guidelines and using the antibodies provided by the kit. Finally, the HRP-based colorimetric reaction was stopped after 10 min, and analyzed in an EnVision Multi-label plate reader (Perkin Elmer).

Live-Cell Microscopy

Live-Cell imaging

For the analysis of neuronal growth rate, 1×10^4 of either WT or RhoA KO neurons suspended in MEM-HS were seeded in a chamber of a 35 mm CELLVIEW 4-well Glass bottom culture dish (Greiner bio-one) for 2 h. Then media was changed to glia-conditioned N2. For the drug treatments, the N2 was supplemented with DMSO 0.01% (vehicle) plus Blebb 0.5 μM or C3T 0.5 μg/ml. After, Differential imaging contrast (DIC) was performed. Images were acquired at 20 min intervals with UApon 40x/1.35 infinity/0.17/FN22 (Olympus).

Cytoskeleton Dynamics

For live-cell imaging of cytoskeleton dynamics, WT and RhoA KO neurons were transfected with a plasmid encoding the expression of both EB3-mCherry and Lifeact-GFP. Then, 5×10^4 of either WT or RhoA KO neurons suspended in MEM-HS were seeded in 35 mm glass-bottom dishes (MatTek) for 2 h. Media was afterward changed for glia-conditioned N2. When indicated, drug treatments were performed as described above. Simultaneous Cherry/GFP images were acquired every 2 s for 2-5 min with a PlanApo 60x/1.42 infinity/0.17/FN26.5 objective (Olympus). All the live-cell imaging experiments were performed on a DeltaVision RT (Applied Precision) based on an Olympus IX71 inverted microscope, with a CO_2 regulated incubation chamber maintained at 37°C (Solent Scientific). Images were acquired with a Photometrics CoolSnap HQ camera (Roper Scientific) using SoftWoRx 3.5.0 imaging software (Applied Precision). The plugins Kymograph_tool and MtrackJ from ImageJ were used for the analysis of actin and microtubule dynamics (NIH)

Whole Brain Clearing and imaging

Brain samples from wild-type and RhoA KO mice were cleared similarly as previously described [38]. Briefly, formaldehyde-fixed brains were sectioned into 2 mm coronal segments and immersed in 15 mL of 50% (v/v with dH2O) ScaleCUBIC-1 Reagent-1A [Urea (25 weight percent (wt%) final concentration), N,N,N,N-Tetrakis(2hydroxypropyl)ethylenediamine (Quadrol, 25 wt% final concentration) and Triton X-100 (15 wt% final concentration), all diluted in bi-distilled water] at room temperature overnight followed by immersion in 15 mL of Reagent-1A at 37°C with shaking for 3 days. Samples were washed with PBS and immersed in 15 mL of 50% (v/v with PBS) ScaleCUBIC-2 [Urea (25 wt% final concentration), Sucrose (50 wt% final concentration) and Triethanolamine (10 wt% final concentration), all diluted in bi-distilled water] at room temperature overnight and then immersed in 15 mL of ScaleCUBIC-2 at 37°C with shaking for 3 days. Coronal sections of the cortex were imaged with a 2-photon microscope (LSM 7MP, Zeiss) equipped with a Spectra Physics InSight X3 laser set at 920 nm and equipped with a 16x Nikon 0.80 numerical aperture (NA), 3.0 mm working distance objective (N16XLWD-PF). Images were 3D-reconstructed for further analysis using Imaris 9.2 software (Bitplane).

Patch clamp electrophysiological recordings

Primary hippocampal neurons of either WT or RhoA KO mice were cultured as described above (neuronal cell culture section) and plated in a density of 88 cells/mm^2. The cells were transferred from the culture medium to a Ringer solution containing (mM) 145 NaCl, 3 KCl, 1 MgCl, 1.5 CaCl2, 10 HEPES, 10 D-glucose (adjusted to pH 7.3 with NaOH). Freshly pulled borosilicate glass pipettes (3-5 MΩ) were filled with an intracellular solution containing (mM) 135 K-gluconate, 10 KCl, 10 HEPES, 0.1 EGTA, 2 MgCl2, 3 K-ATP, 0.3 Na-GTP (adjusted to pH 7.2 with KOH). Recordings were carried out at 31-32°C controlled by Temperature Controller VII (Luigs-Nemann) in flowing Ringer solution. MultiClamp 700B was used to amplify and AxonDigidata 1550B was used to digitize (10 kHz sampling rate) the signals (both from Molecular Devices). Basic physiological membrane properties were assessed including resting membrane potential (measured in current clamp mode) and membrane input resistance (calculated based on voltage deflection in response to negative current injections). Spontaneous excitatory postsynaptic currents (sEPSCs) were measured in voltage clamp mode for

one minute with a holding potential of −60 mV. sEPSC detection was carried out with the Axon clampfit 11 template search tool (Molecular Devices).

QUANTIFICATION AND STATISTICAL ANALYSIS

Quantification

Data analysis was performed as follows: In culture experiments (Figures 3B–3L, 5A–5E, 7F, 7G, S2G, S3B–S3D, S3H, S3I, S4A–S4D, and S5A–S5F), neurons without neurites or showing neurites shorter than 10 μm were considered as stage 1 (no neurites). Neurons showing neurites longer than 10 μm without medial-to-distal accumulation of Tau-1 were considered as stage 2 (not polarized). A neurite displaying a medial to distal accumulation of the axonal marker Tau-1 was considered an axon. Neurons that elaborate an axon were stage 3 (polarized). Neurons exhibiting multiple axons were also considered stage 3 neurons. Total axon length refers to the length covered by the main axon shaft plus its branches.

To analyze axon growth in time-lapse video-microscopy (Figures 5F–5H), the axon of the neurons is identified at the end of the video, the video is rewind and the length of the neurite that originated it was measured over time using ImageJ. In this experiment, only the length of the main axon shaft was analyzed.

To resolve the kinetic components of axonal growth (Figures 5G, 5H, and S3J), a custom-made script (see Key Resources Table) was generated to detect growth events (one or more followed events resulting in length increases > 5 μm with tolerance for single intermediate drop event < 1 μm), retraction events (one or more followed events resulting retractions > 5 μm in length with tolerance for single intermediate increase event < 1 μm) and pause events (considered as followed events with length variations < 0.1 μm).

In culture cell experiments where axonal markers were not employed, the longest neurite of the neuron, at least 50 μm long, was considered the axon (Figures 4G, 4H, 4M, 4N, 6D–6F, 7A–7E, S4E–S4J, S5G, and S5H).

In experiments where we study the formation of actin arcs in growth cones (Figures 6D, 6E, S4E, S4F, S5G, and S5H) we considered that a growth cone contained actin arcs when transversal actin dense structures, perpendicular to the exe of microtubule growth, were present and microtubules showed preferential retention within the P-domain.

The density and extension of axon from electroporated neurons in cortical slices (Figures 2B and 2C) were determined as follows: The limit of the electroporated area was defined as the region where the fluorescent signal is below 10% of the maximum intensity of the whole electroporated area. Starting from this limit, a ROI was created containing the axons exiting caudally from the IZ (Figure 2C, diagram). The images were then processed to transform the fluorescent signal of axons into binary lines independent of the amount of fluorophores expressed by individual axons. For this, we used a macro containing the following functions from ImageJ: Tubeness/Gaussian blur/Binary mask/Skeletonize. The resulting images were analyzed with the linescan/plot profile tools of ImageJ to determine the density of axons as the measured signal intensity. We performed this analysis for 2 consecutive brain slices to better span the entire electroporated area and the values were averaged. Note that in one of the RhoA KO brains, three consecutive slices were required for the analysis. Followed, we calculated the average distance covered by axons emanating from the electroporated region (ER) for each brain. Then, we calculated the groups mean variance between WT and KO axons and the variance within treatments. The resulting data were analyzed with a Custom ANOVA test (F-test). For all images, a corresponding mask of DAPI staining was used to correct for ruptures and discontinuities in the tissue.

In organotypic cultures derived from ex utero electroporations (Figures 2D–2F), we started the time counting when a neuron showed the first signs of MP morphology and terminated when the neuron acquired a stable BP morphology. We considered the end of the MP-BP transition of neurons as the onset of neuronal polarity.

To determine the presence and number of axon per neuron (polarity) in the cortex and hippocampus of cleared adult brains (Figures 1D–1F) as well as in the cortical plate of embryonic brains derived from in utero electroporations (Figures S1A and S1D), we counted all neurons in selected regions and sorted them in two groups: 1) neurons "with single axon," those neurons displaying long axons or showing a clear bipolar morphology (showing leading and trailing processes), and 2) with "no axon detected," where by reasons of low reporter signal or tissue damage we could not determine unambiguously the presence or absence of an axon or trailing process. Therefore, we cannot exclude that a neuron labeled "no axon detected" may indeed have an axon. In none of the cases we found a neuron with more than one axon.

Statistical Analysis

Statistical analysis was performed using Prism (v. 6.0; GraphPad Software) as follows: unpaired two-tailed Student's t test (Figures 1E, 1F, 2F, 4B, 4D, 4F, 4H, 4J, 4L, 4N, 6C, 7D (black asterisks), S1D, S3H, S4A–S4D, S4F–S4H, S4J, and S5H); Mann-Whitney-test (Figures S2D and S2E); multiple comparison by one-way ANOVA with Tukey's post-test (Figures 3H, 3J, 3L, 5H, 6E, 6F, 7D (red asterisks), 7G, S2G, S3C, S3D, S3I, S3J, S5B, S5C, S5E, and S5F); ordinal logistic regression integrating time progression and correction for experimental variability (Figures 3C, 3E, 5B, and 5D; see Key Resources Table); generalized linear model (GLM) using a Gamma distribution to account for the non-negative range of the length plus correction for confounding effects of the individual experiments (Figures 3D, 3F, 5C, and 5E; see Key Resources Table); two-way ANOVA with Tukey's post-test (Figures 5G and 7E); customized ANOVA test (F-test) (Figure 2C; see Key Resources Table); custom-made Fisher's permutation test corrected for multiple comparison error by Benjamini-Hochberg procedure ([93]; see Key Resources Table) (Figure S1B). For all analyses performed, significance was defined as *$p < 0.05$; **$p < 0.01$; ***$p < 0.001$ and ns, not significant.

DATA AND CODE AVAILABILITY

The datasets supporting the current study have not been deposited in a public repository. The reported data are archived on file servers at the German Center for Neurodegenerative Diseases (DZNE) and are available from the corresponding author on request. Permutation test was performed using a custom script ''permutation_test 0.18'' implemented in Python (2.7.3 version) including Pandas and NumPy libraries. The script is available for download in the Python Package Index (https://pypi.org/pypi/permutation_test). Custom ANOVA test (F-test) is available from download at SciPy.org (http://www.scipy.org/). The script for Generalized linear model (GLM) can be accessed from the R Project for Statistical Computing (https://www.R-project.org/.). The custom-made Axon growth kinetics script for Phyton can be downloaded from (https://nextcloud.dzne.de/index.php/s/AeOZTNgco8rxp1j/download).